Polyphase deformation and deformation-magmatism interaction in the Pan-African 4°50' shear zone (Hoggar, Southern Algeria)

Aboubakr Deramchi, Alain Vauchez, Abderrahmane Bendaoud, Fabrício de Andrade Caxito, Zakaria Boukhalfa, Sidali Doukkari, Saïd Maouche, Cristiano Lana, Khaled Aghanbilou, Abderrezak Bouzid

This article was initially published in the Elsevier journal "Precambrian Research. The published version can be seen at https://doi.org/10.1016/j.precamres.2023.107085

Polyphase deformation and deformation-magmatism interaction in the Pan-African 4°50′shear zone (Hoggar, Southern Algeria)

Aboubakr Deramchi [a,*], Alain Vauchez [b], Abderrahmane Bendaoud [c], Fabrício de Andrade Caxito [d], Zakaria Boukhalfa [a], Sidali Doukkari [c], Saïd Maouche [a], Cristiano Lana [e], Khaled Aghanbilou [a], Abderrezak Bouzid [a]

[a] *CRAAG, BP 63, Route de l'Observatoire, Algiers 16340, Algeria*
[b] *Géosciences Montpellier, Université de Montpellier, CNRS, 34095 Montpellier, France*
[c] *LGGIP, FSTGAT, USTHB, BP 32, Al Alia, Dar el Beïda, Algiers 16123, Algeria*
[d] *IGC–CPMTC, Universidade Federal de Minas Gerais, Campus Pampulha, 31270-901 Belo Horizonte, MG, Brazil*
[e] *Departamento de Geologia, Universidade Federal de Ouro Preto, Campus Morro do Cruzeiro, 35400-000 Ouro Preto, MG, Brazil*

A B S T R A C T

The 4°50′Shear zone (SZ), one of the major structures of western Gondwana, formed in Hoggar during the Pan- African orogeny is still poorly studied; especially ages and deformation characteristics are lacking. We performed microstructural analysis and EBSD measurements on nine selected mylonites from the 4°50′SZ, and zircon U-Pb dating on two granitoid samples. The protolith of these mylonites are granitoids. Most samples display segre-gation of dominant feldspar and minor quartz in separate layers that underline the N-S subvertical mylonitic foliation. Feldspar grains display evidence of intracrystalline deformation, supporting dextral shear-sense. Plagioclase and K-feldspar are frequently corroded with embayments infilled by secondary K-feldspar and plagioclase respectively. Interstitial quartz grains disseminated in feldspar aggregates may infill fractures in feldspar grains. Quartz ribbons, usually parallel to the foliation, locally crosscut feldspar layers. Quartz is partially recrystallized and elongate crystals form a secondary foliation at ~ 30° to the main foliation, supporting a later sinistral shearing. In some samples, amphibole is associated with quartz and oriented parallel to the foliation. In all samples, quartz CPO suggests a dominant prism-<a > slip-system, activated at medium/high temperature (~500-700°c), but stress-induced oriented crystallization may have contributed to this CPO. K- feldspar CPO supports the activation of the [100](010) slip system while the plagioclase CPO points to acti-vation of [100](001) system. These CPO support dislocation creep under amphibolite facies conditions. These new data, in addition to U-Pb dating, suggest the following evolution: 1) successive intrusions of granitoids in the SZ (~661-~639 Ma) due to partial-melting of the lower-crust and, possibly also of the lithospheric-mantle, 2) the 4°5 0′SZ was rooted in the lower-crust or the upper-mantle, and 3) dextral shearing lasted over ≥ 20My. This was followed by successive magma batches that intruded these rocks during a late migmatitic episode (~623-~609 Ma). After ~ 609 Ma, a moderate sinistral reactivation of the 4°50′SZ occurred and was accommodated through dislocation creep mainly localized in quartz ribbons. During accretion of the Western Gondwana, the 4°50′SZ was active during subduction. During ≥ 20My, it was successively intruded by granitoids that cooled down slowly, and have been deformed in the submagmatic state then in the solid-state.

1. Introduction

The 4°50′ shear zone (SZ) in the Hoggar has been considered as the northern segment of a transcontinental shear zone involving the Kandi and Transbrasiliano shear zones respectively in the African and South-American continent (Fig. 1A; Cordani et al., 2013; Ganade de Araujo et al., 2014; Caxito et al., 2020). Such major shear zones likely represent lithospheric shear zones (Caby, 2003; Liégeois et al., 2003, 2005; Vauchez et al., 2012; Bouzid et al., 2015). They significantly contributed to the deformation associated to the building of the Gondwana supercontinent.

During the Neoproterozoic, the Pan-African orogeny affected many

* Corresponding author.
E-mail address: aboubakarderamchi@gmail.com (A. Deramchi).

Archean/Paleoproterozoic terranes that form the present Tuareg Shield. The 4°50′ SZ, which is one of the largest shear zone of the Tuareg Shield, separates Central Hoggar from Western Hoggar and played an important role in the structuration of the Hoggar during the Pan-African orogeny (*e.g.,* Caby, 2003; Liégeois et al., 2003). The Central Hoggar was affected by this orogeny. The western part of the Central Hoggar preserved above all of what occurred in pre-Neoproterozoic a memory of what happened during the late Neoproterozoic and even lately. The intrusion of some granitoids in the crust during the late Neoproterozoic was related to the 4°50′ SZ (*e.g.,* Djouadi et al., 1997). However, the relationships between their emplacement and the strain evolution of the shear zone are currently not well constrained by structural/microstructural work. Indeed, no detailed studies of the deformation processes and of the relationships between deformation and magmatism have been done yet. Here, we present for the first time microstructural and fabric data (Electron Backscatter Diffraction - EBSD - measurements) to characterize the deformation of crustal mylonites that outcrop in the 4°50′ SZ, the interaction with the latter, and the geodynamical processes accommodated by this tectono-magmatic system. In addition, we have acquired U-Pb zircon ages on three mylonitic samples that provide additional information on the evolution of the Pan-African orogeny.

2. Geological Setting and rock description

2.1. Geological setting

The pre-Gondwana fit between the NE Brazil and the NW Africa is substantiated by the marine magnetic anomalies of the South Atlantic Basin (*e.g.,* Le Pichon, 1968) and the Braziliano/Pan-African orogeny present in both continents (*e.g.,* Caby, 1989; Ganade de Araujo et al., 2014). During this orogeny, the continuity of major shear zones between the Brazilian and African domains played an important role in the building of the orogen (*e.g.,* Vauchez et al., 1995; Caxito et al., 2020). This transcontinental system is ~6000 km long and involves the Transbrasiliano (Brazil), Kandi (Benin and Togo), and 4°50′/Iskel SZ (Hoggar) (Le Pichon, 1968; Arthaud et al., 2008; Cordani et al., 2013; Ganade de Araujo et al., 2014; Santos et al., 2015; Brahimi et al., 2018; Deramchi et al., 2020).

Here we focus on the 4°50′ SZ as it represents a major component of the Pan-African orogeny in Hoggar and may provide new insights on the formation of Gondwana.

The Hoggar in Algeria is the largest domain of the Tuareg Shield (Fig. 1a). The Tuareg Shield, composed of Archean and Proterozoic

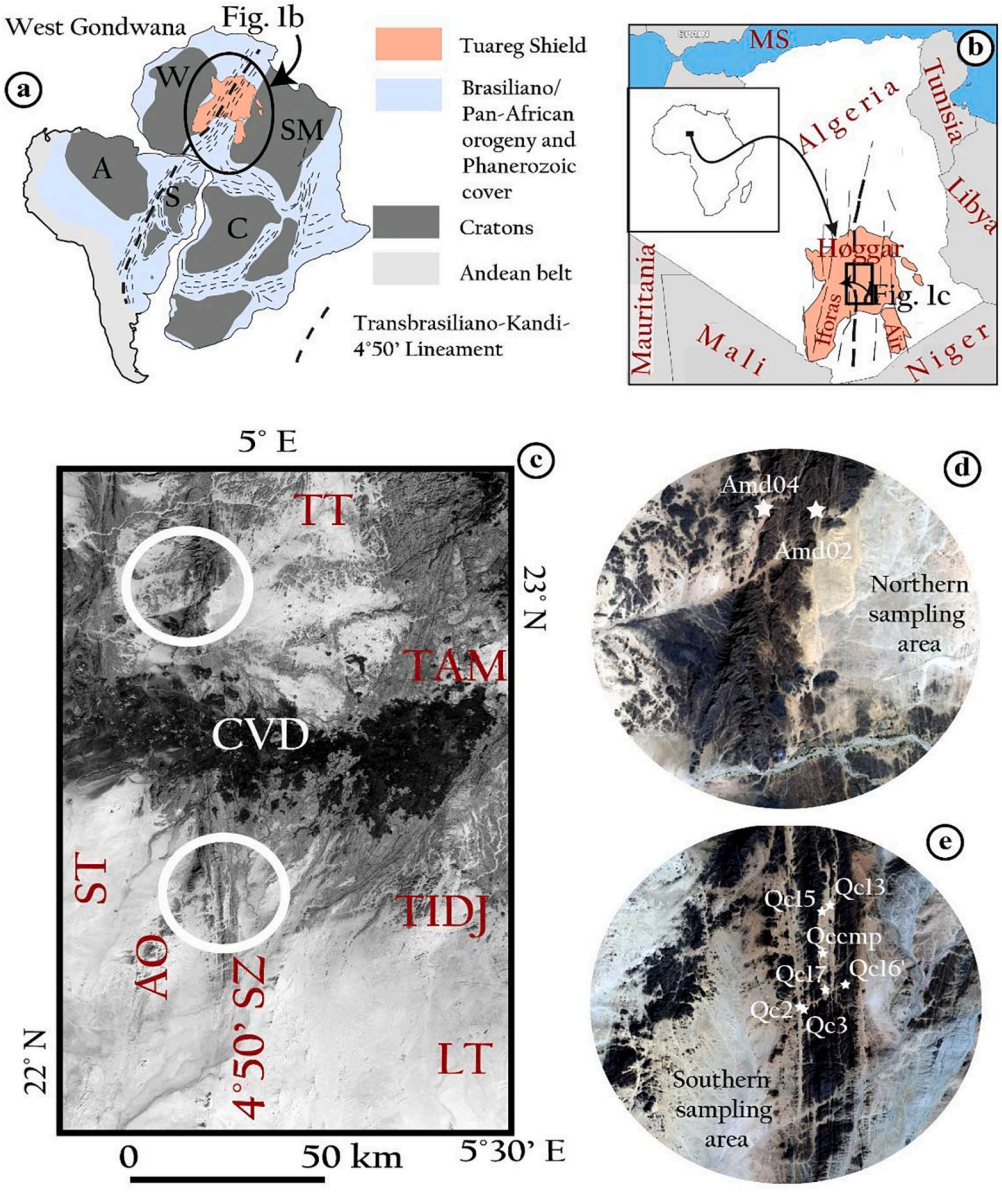

Fig. 1. Location of the study area at the Gondwana scale. a. Sketch map of the West Gondwana Orogen showing the location of the Tuareg Shield (modified from da Silva Amaral et al., 2023). **A**: Amazonian craton. **W**: west African craton. **SM**: Saharan metacraton. **C:** Congo craton. **S:** São Fransisco craton. **b.** Geographic location of the study area in the Tuareg Shield. **MS:** Mediterranean Sea. **c.** Landsat 8 image showing the 4°50′ shear zone in the Tuareg Shield. **LT**: Laouni terrane; **TAM**: Tamanrasset town; **TIDJ**: Tidjenouine; **TT**: Tefedest terrane; **CVD**: Cenozoic volcanic district; **ST**; Silet terrane; **SZ**: Shear zone. White circles show the northern and the southern sampling areas of both segments of the 4°50′E shear zone. **d.** Adapted zoom to the northern sampling area. **e**. Zoom to the southern sampling area. White stars show the samples localization.

terranes (*e.g.*, Ferré et al., 1996, has been widely deformed during the Pan-African orogeny (750 – 550 Ma. The amalgamation of these terranes during this orogeny occurred through the closure of several paleo-oceans and involves island arc accretions, collisions between continental blocks, and transcurrent movements along major shear zones (*e.g.*, Ferré et al., 2002; Bouzid et al., 2019; Liégeois, 2019; Boukhalfa et al., 2020; Deramchi et al., 2020; Araïbia et al., 2022; Ouadahi et al., 2022. The West Ouzzalian-, Adrar-, Iskel-, 4°50'-, Ounane- and Raghane-SZ are the most important shear zones that have been interpreted as sub-meridian transcurrent SZ and, for some, as putative suture zones separating these continental blocs (Fig. 2a; Caby, 2003; Liégeois et al., 2003; Brahimi et al., 2018; Liégeois, 2019; Deramchi et al., 2020; Boukhalfa et al., 2020; Araïbia et al., 2022; Ouadahi et al., 2022). The 4°50′ SZ separates the LATEA micro-continent from the Silet terrane north of the Cenozoic volcanic district (Fig. 2a and delimits the westernmost terrane of the LATEA (Aouilène terrane) south of it. LATEA is defined as a micro continent comprising five Archean to Paleoproterozoic terranes, namely: Laouni, Azrou-n-fad, Tefedest, Egéré-Aleksod and Aouilène (Black et al., 1994; Liégeois, 2019). This microcontinent is composed of Archean to Paleoproterozoic migmatitic/gneissic formations covered by Paleoproterozoic to Neoproterozoic sedimentary and magmatic rocks (Liégeois et al., 2003; Ouzegane et al., 2023). High-temperature peak-metamorphism is known in the Tidjenouine area in the southern part of LATEA (Fig. 2a) with 860 ± -50 °C and 0.7–0.8 GPa PT conditions at 2062 ± 39 Ma (ICP-MS U-Pb in zircon) and also > 700° C and 0.4−0.3 GPa at 614 ± 11 Ma (Bendaoud et al., 2003; 2008). High-pressure rocks >1.5 GPa −790° C (eclogites) have been described in Laouni, Azrou-n-fad and Egéré-Aleksod terranes (Sautter, 1986; Liégeois et al., 2003; Arab et al., 2014; Doukkari et al., 2014; Doukkari et al., 2015; Bruguier et al., 2020) and have been dated at ~655 Ma (Bruguier et al., 2020) and 680–630 Ma (Ouzegane et al., 2023).

In addition, Boullier and Bertrand, 1981 suggested that earlier Pan-African thrust tectonics was lately followed by vertical strike slip faulting. These deformation episodes under contrasted high-grade

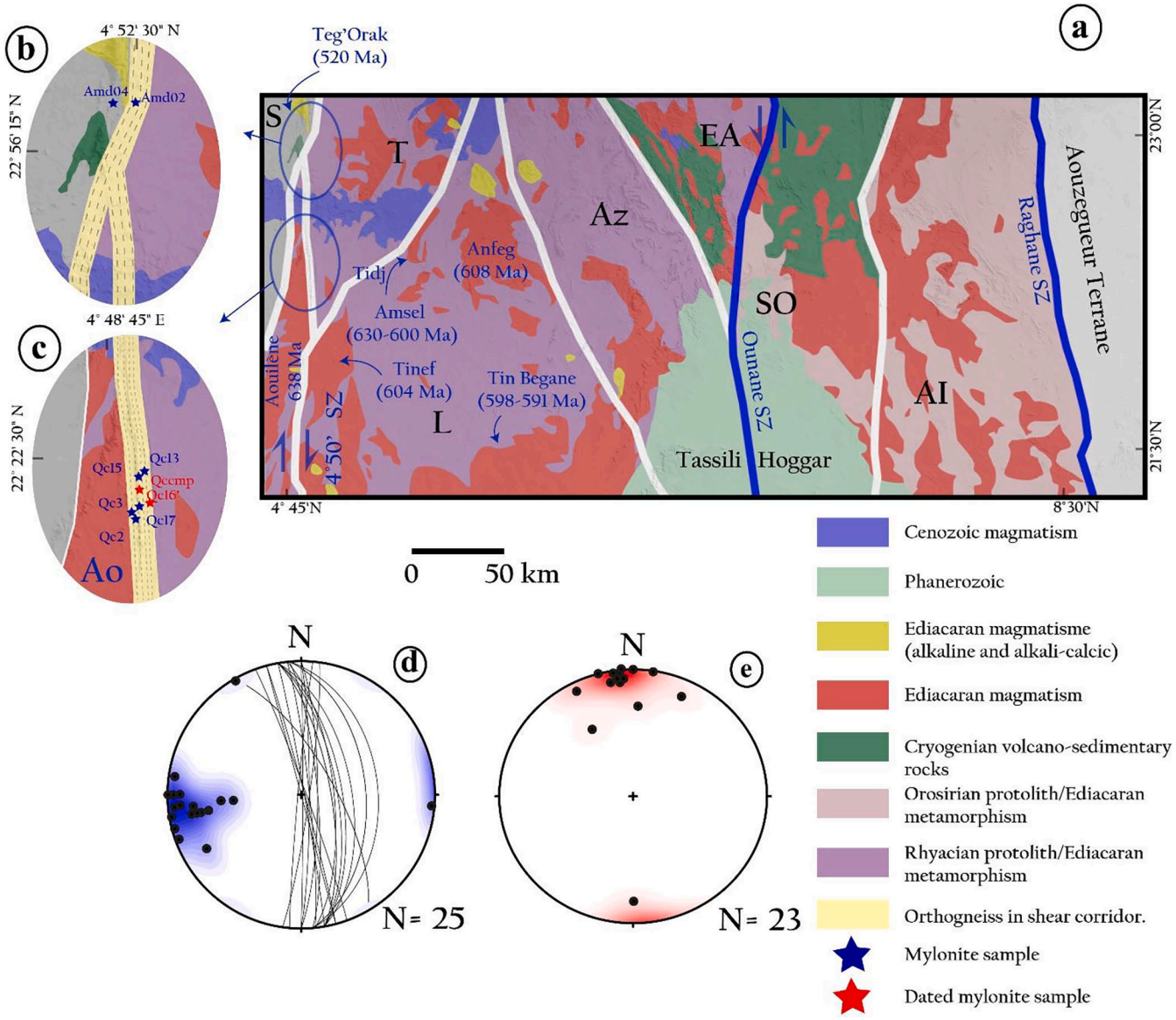

Fig. 2. Location and structure of sampled outcrops: a. Localization of the granitic batholiths in the adjacent terranes and kinematic overview of both limits of LATEA (modified from Liégeois, 2019). b. Simplified geological map of the northern sampling area. c. Simplified geological map of the southern sampling area. d. Foliation planes and poles orientation, lower hemisphere and equal angle data projection plotted in Stereonet 11. e. Stretching lineation orientation, data plotted in lower hemisphere and equal angle. AI: Assodé-Issalane terrane; AZ: Azrou 'n'fad terrane; EA: Egéré-Aleksod terrane; L: Laouni terrane; SO: Serouanout terrane; S: Silet terrane; SZ: Shear zone; Tidj: Tidjenouine; T: Tefedest terrane.

metamorphic conditions support that LATEA underwent several orogenic episodes during the Precambrian. West of LATEA, the Silet terrane was defined as a greenschist-deformed island arc (Black et al., 1994; Azzouni-Sekkal et al., 2003; Caby, 2003; Béchiri-Benmerzoug, 2012.

Recent geophysical and geological/geochemical investigations confirm that the suture between LATEA and Western Hoggar is located further West (Iskel shear zone; Brahimi et al., 2018; Liégeois, 2019; Deramchi et al., 2020; Ouadahi et al., 2022. On the other hand, the 4°50′ SZ exhibits high electrical conductivity values but has not been considered as a suture zone (Bouzid et al., 2019; Deramchi et al., 2020. LATEA and Silet terranes are located on the eastern part from the Iskel suture zone, while In Teïdeni (partially and Tin Zaouatene terranes are located on its western side and are considered as a likely Archean, Paleoproterozoic (Deramchi et al., 2020 or Mesoproterozoic sliver (Ouzegane et al., 2023.

On both sides of the 4°50′ SZ, abundant magmatic intrusions which are close to the shear zone in LATEA and Silet and are principally related to the Pan-African magmatism controlled by the 4°50′ SZ (Azouni-Sekkal et al., 2003; Bechiri-Bemerzoug, 2012 and 2017; Bettioui et al., 2022. These magmatic bodies were emplaced since the Ediacaran-Cambrian time periods (Caby et al., 1982; Azzouni-Sekkal et al., 2003; Azzouni-Sekkal et al., 2020; Bechiri-Benmerzoug, 2012; Bechiri-Benmerzoug et al., 2017.

Bechiri-Benmerzoug, (2012 and 2017) suggested that west of the 4°50′ SZ, several granitoid batholiths emplaced from the Tonian (868 ± 4 and 742 ± 5 Ma) to the Cryogenian (651 ± 6 and 638 ± 5 Ma) are related to subduction. These granitoids are mainly tonalitic, granodioritic, and monzogranitic. They show a typical TTG composition and decrease in age from West to East, with the most recent one (Anou-Eheli batholith, 638 ± 5 Ma) located in the Aouilène terrane. Trace elements and isotope geochemistry suggest that this latter derive from an old continental crust, from which it conserved its TTG characteristics, but was contaminated with LATEA crust (Bechiri-Benmerzoug, 2012).

Eastward of the 4°50 'SZ sampling areas, numerous highly potassic calc-alkaline (HKCA), granitoids, mostly 630 to 580 Ma in age, outcrop (Acef et al., 2003; Liégeois et al., 2003; Abdallah, 2007; Bowden et al., 2014; Bouzeguella-Talmat, 2014; Bettioui et al., 2022). These granitoids are interpreted as post-collisional and related to Pan-African transcurrent displacements along sub-vertical mega-shear zones (Liégeois et al., 2003; Acef et al., 2003).

For instance, in the Laouni terrane, the Anfeg batholith (Fig. 2a) (608 Ma) displays a mixed signature between an old continental Paleoproterozoic crust (1.9 Ga or older) and a depleted mantle (Acef et al., 2003). The Tinef (Fig. 2a) batholith exhibits also a similar age at 604 Ma (Bertrand et al., 1986). The Anfeg (Fig. 2a) batholith displays similar isotopic signature to the Anou-Eheli batholith (Bechiri-Benmerzoug, 2012). Further south, the HKCA Tin Begane batholith (Fig. 2a), essentially crustal in origin, shows younger ages ranging from 598 ± 3 Ma to 591 ± 6 Ma with zircon mainly inherited from the Paleoproterozoic and Cryogenian (Bettioui et al., 2022). Its emplacement occurred in an extensional tectonic context and was related to a detachment zone associated to the northward tectonic escape of the Tuareg Shield (Fettous et al., 2018; Bettioui et al., 2022).

Migmatization in LATEA is regarded as the source of quartzo-feldspathic layers with amphibole and biotite (Fettous et al., 2018; Bettioui et al., 2022). High-temperature metamorphism with partial melting of ancient material around 600 Ma is documented (Bendaoud et al., 2008; Bowden et al., 2014; Fettous, 2016; Bettioui et al, 2022).

Many highly-potassic calc-alkaline granitoids were emplaced due to the reactivation of the major shear zones (630 to 580 Ma; Abdallah et al., 2007; Liégeois et al., 2003). Afterwards, alkaline and alkali-calcic subcircular granitoids (Taourirt) intruded the Hoggar during the late Ediacaran to early Cambrian (584 – 520 Ma) (Azzouni-Sekkal et al., 2003; Azzouni-Sekkal et al., 2020) and especially along submeridian shear zones in Silet and LATEA terranes. These post-collisional to post-orogenic granitoids resulted from partial melting of an enriched mantle source contaminated with an old continental crust (Azzouni-Sekkal et al., 2003). Tesnou and Teg'Orak (Fig. 2a) Taourirt plutons are located at the western edge of the 4°50′ SZ. Both plutons were emplaced by ~ 540 Ma (Azzouni-Sekkal et al., 2003; Azzouni-Sekkal et al., 2020) and display a well-defined magnetic fabric associated to a dextral shearing episode of the 4°50′ SZ (Henry et al., 2008, 2018).

In the southern sampling domain, the shear zone is ~10 km wide (Fig. 1b) while in the northern one, it is narrower ~ 5 km. In both segments, the 4°50 E SZ displays a strong N-S foliation at the satellite image scale (Fig. 1), and rocks outcropping inside the SZ show an N-S trending orientation (Fig. 3). On both sides of the 4°50′ SZ, the regional foliation, likely Pan-African in age, is rather oriented NE-SW and curves to N-S when reaching the shear zone in agreement with a sinistral shear sense.

The dextral shearing in the 4°50′ SZ is interpreted to be Pan-African to early Phanerozoic (Boullier and Bertrand, 1981; Caby, 2003; Guiraud et al., 2005). Several reactivations of this major shear-zone have been substantiated by various authors. According to Guiraud et al. (2005), the 4°50′ SZ underwent dextral shearing reactivation in the early Cambrian period (545–495 Ma). Transpressional reactivation of the 4°50′ SZ is also documented in the Ordovician (Beuf et al., 1971; Boudjema, 1987). Thereafter, a sinistral shear movement of the N-S Hoggar major shear zones is defined during early Devonian (416 – 392 Ma). A dextral shear sense occurred betwen the Stephanian and the early Permian (304 – 256 Ma). During the Mesozoic, sinistral strike slip faulting reactivated the 4°50′ SZ (142 – 120 Ma; Guiraud et al., 2005) likely related to the break-up of Western Gondwana. During the Cenozoic, especially the early to late Eocene, sinistral faulting reactivated the 4° 50′ SZ likely linked to the beginning of the shield exhumation in response to the sudden slowdown of the African plate (Rougier et al. 2013) due to the Africa-Europe collision (Liégeois et al., 2005).. Sinistral sense of movement is also known during the Pliocene-Quaternary (5.3–0 Ma; Guiraud et al., 2005).

Altogether and for most major shear zones of the Tuareg Shield (*e.g.,* Liégeois et al.; Bouzid et al., 2015), these reactivations indicate that the 4°50′ SZ represents a long-lived fault, active from the Pan-African to the Quaternary.

2.2. *Rock description*

Sampling was based on choosing the rocks that are the most representative of the rock-type and microstructure within the 4°50′ SZ. In the southern part of the 4°50′ SZ (Fig. 2c), we have sampled the eastern, middle, and western parts of the shear zone (QC02, QC03, QC13, QC15, QC16′, QC17 and QCCMP; Fig. 1e and 2b). North of the volcanic district (Fig. 1d and 2b), two samples were taken for comparison purpose (AMD02, AMD04).

In most cases, they are characterized by dominant K-feldspar and plagioclase layers and minor quartz layers, which define the ~ NS mylonitic foliation. Locally, amphibole and biotite crystals are also present and oriented parallel to the foliation. On the foliation planes, elongated crystals, especially K-feldspar (Kfs) and amphibole when present define a N-S sub-horizontal mineral stretching lineation (Fig. 3a and e). At the outcrop scale, ductile deformation is also highlighted by many mesoscale structures such as intrafolial folds, C-S fabric, lenticular clasts, and asymmetric tails on feldspar (Fig. 3). Some textures are migmatitic (Fig. 3f). Altogether, these structures point to a significant deformation and dominant dextral shearing (Fig. 3a and b).

The foliation of the 4°50′ shear zone mylonites does not show marked variation between the sampled outcrops, it is oriented ~ N350E with a sub-vertical to vertical dip (*e.g.* 70-90°). The lineation is sub-horizontal or dips gently to the North (Fig. 3a, d, f). This vertical foliation is locally crosscut by NE-SW and NW-SE shear zones that likely occurred later under relatively lower temperature with dextral and sinistral shear senses, respectively. It also displays evidence of

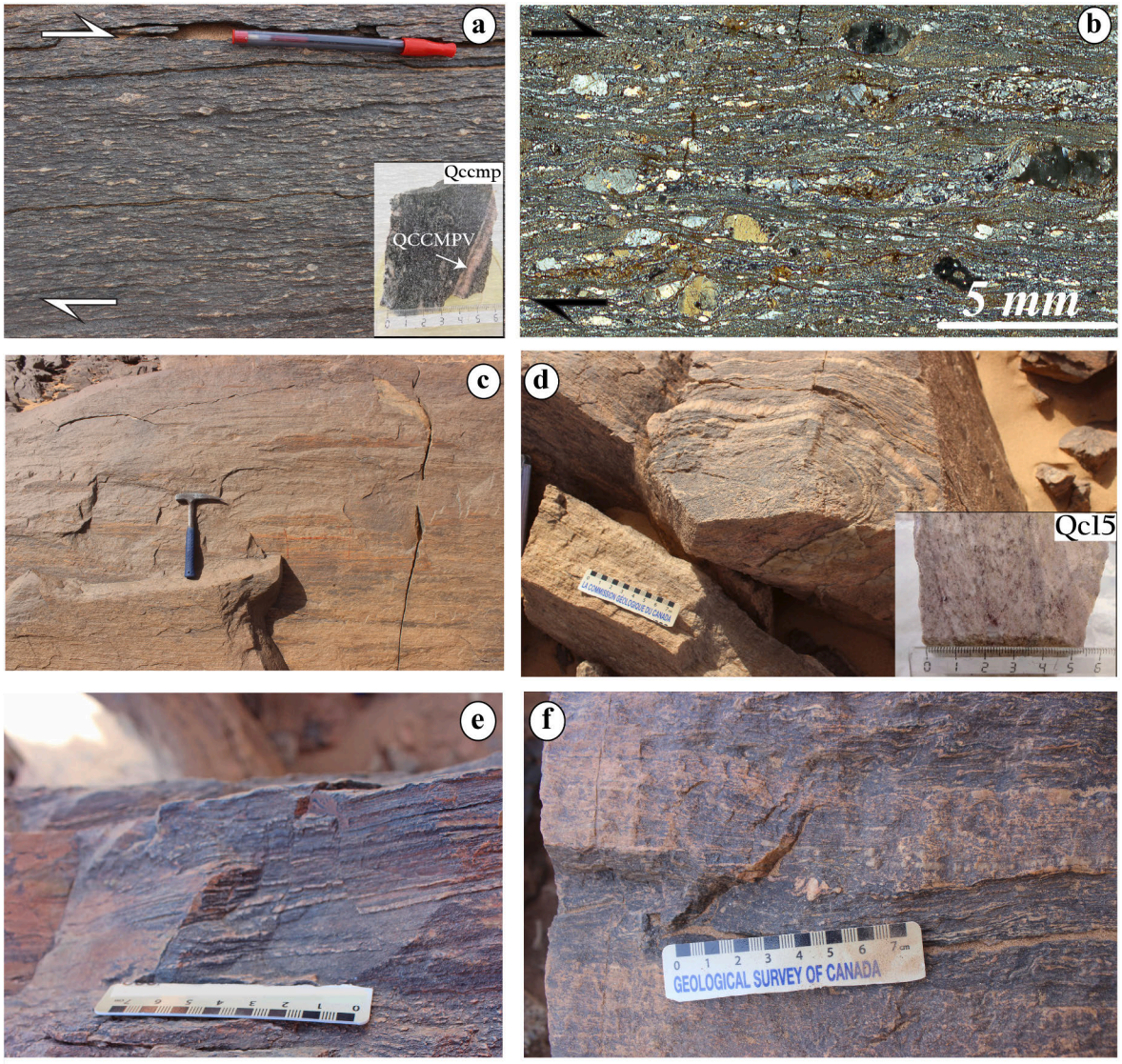

Fig. 3. Macroscopic structures of the studied outcrops: a. Asymmetric feldspar porphyroclasts indicating a dextral shear sense in the QCCMP. b. Section of QC10 sample (from thin section) showing dextral shearing. c. Horizontal striation on the mylonitic foliation plane. d. Alternating layers of leucosome folded in a late fold. e. Late small extensional brittle fault cutting the layers that mark the mylonitic foliation. f. Feldspar porphyroclast rotated in the folded primary foliation.

superimposed ductile and brittle deformation (Fig. 3e). Many N-S vertical brittle faults planes bearing horizontal striation were observed and these coexist with ductile lineation at the same outcrop (Fig. 3c) and are respectively parallel to the foliation plane and mineral stretching lineation.

Felsic dykes (age unknown), exposed in the central part of the southern domain, are also mylonitized (QC13 and QC17 sample), as the other rocks. These thin dykes (~0.5 m wide) present similar N-S oriented foliation and lineation as the other samples. This suggests that all the rock types outcropping in the two sampled domains of the 4°50′ shear zone have been deformed during at least one common tectonic episode.

2.3. Composition of studied samples

All the samples are mylonitized and show modal variation from a sampled outcrop to the other. Modal composition has been estimated from EBSD mapping that covers almost entirely the thin sections. All samples contain dominant Kfs and plagioclase. Samples located in the northern sampling area (Fig. 1d and 2b) are plagioclase-rich (one monzogranite and one tonalite) while those from the southern domain are richer in Kfs (3 syenogranite and 4 monzogranite). Only the monzogranite Qccmp sample, from the center part of the 4°50′ shear zone in the southern domain (Fig. 1e and 2c), has a higher quartz content than the other samples. However, for all of them the protolith is of magmatic origin.

3. Methods

3.1. Electron Backscatter Diffraction

Electron Backscatter Diffraction (EBSD) analysis was used to map the rock-forming minerals of each mylonitic sample and measure their crystallographic preferred orientation (CPO). Thin sections were cut perpendicular to the foliation and parallel to the lineation. They were carefully polished to get an enhanced mapping during acquisition. EBSD measurements were performed in the JEOL JSM-5600 scanning electron microscope (SEM_EBSD) at Geosciences Montpellier (Université de Montpellier-France) with an acceleration voltage of 17 kV and a working distance of 23 mm. The acquisition step was 15 or 27 μm depending on the grain size.

EBSD data processing was performed using the Aztec data

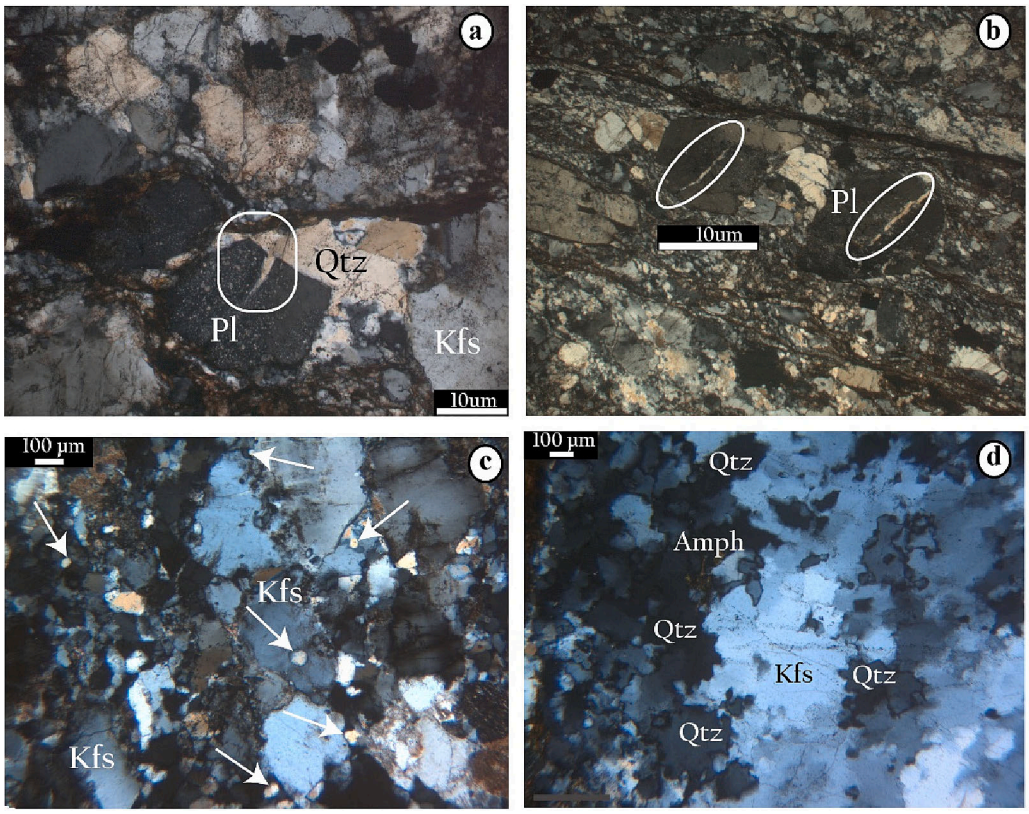

Fig. 4. Microstructures of studied samples. 1: a and b. Submagmatic fractures in plagioclase filled by quartz. In a), the quartz filling the submagmatic fracture is connected to a large quartz grain outside the plagioclase. c. Scattered and interstitial quartz grains between and inside the feldspar grains. d. Curved boundaries of the quartz grains corroding potassic feldspar.

acquisition software (HKL technologies, Oxford instruments). EBSD maps covered about 80% of the thin sections surface. The orientation of grains was recorded using the Euler angle convention. Noise reduction correction was performed with the Flamenco software to improve the resolution of the EBSD maps.

EBSD maps and Crystallographic Preferred Orientations (CPO) data were produced using the MTEX toolbox in MATLAB (https://mtex-toolbox.github.io/; Hielscher & Schaeben, 2008; Bachmann et al., 2010; Bachmann et al., 2011; Mainprice et al., 2014). All pole figures were generated through lower hemisphere equal area stereographic projections, contoured using a half width of 10° and a cluster size of 2°. Contouring is in Multiple of Uniform Distribution (MUD).

3.2. U–Pb (Zircon)

U–Pb LA-ICP-MS (Laser Ablation – Induced Coupled Plasma Mass Spectrometry) analysis (in supplementary material 2 and 3) were performed in zircon crystals separated through standard crushing, sieving, magnetic and gravimetric methods from homogeneous portions in the SEPURA – Laboratório de Separação Mineral de Alta Pureza at CPMTC, UFMG – Federal University of Minas Gerais, Brazil. After mounting in epoxi and polishing, zircon crystals were imaged through standard SEM (Scanning Electron Microscopy) techniques such as Secondary Electrons (SE), Back-Scattered Electrons (BSE) and Cathodoluminescence (CL).

Zircon U–Pb isotope analyses were performed by LA-ICP-MS at Federal University of Ouro Preto (UFOP) using a Thermo-Fisher Element II sector field ICP-MS coupled to a CETAC LSX-213 G2+ ($\lambda = 213$ nm) Nd:YAG laser. A detailed description of the method is given by Gerdes and Zeh (2006, 2009). Ablation was carried out in a low-volume cell with He as carrier gas; laser beam parameters used were a spot size of 20 µm, a repetition rate of 10 Hz, and a fluence of ~3 J cm-2. Time-resolved raw data were corrected offline for background signal, common Pb, laser-induced elemental fractionation, instrumental mass discrimination, and time-dependent elemental fractionation of Pb/U using the GLITTER® software package (Van Achterbergh et al., 2001). Common Pb correction was applied using the interference- and background-corrected 204Pb signal and a model Pb composition (Stacey and Kramers, 1975). Laser induced elemental fractionation and instrumental mass discrimination were corrected by normalization to the reference zircon GJ-1 (Jackson et al., 2004), which was routinely measured within each analytical session. The drift in inter-elemental fractionation (Pb/U) during 30 s of sample ablation was corrected individually before normalization to GJ-1. Reported uncertainties (2σ) were propagated by quadratic addition of the external reproducibility obtained from the standard zircon GJ-1 (Jackson et al., 2004) during the analytical session (2SD in %) and the within-run precision of each analysis (standard error in %). To test the validity of the applied methods and the reproducibility of the data, multiple analyses of the reference zircon Plesovice (337.3 ± 0.4 Ma 2σ, Sláma et al., 2008) were performed. In addition, several analyses of the in-house reference zircon BB (560.0 ± 0.4 Ma 2σ, Santos et al., 2017) were conducted. All uncertainties are presented at the 2σ level. Samples were analyzed in two sessions. In the session were sample QC16 was analyzed, BB and Plesovice returned Concordia ages of 558.2 ± 4.5 Ma and 337.0 ± 2.6 Ma, respectively. In the session were samples QCCMP and QCCMPV (xenolith in QCCMP) were analyzed, BB and Plesovice returned Concordia ages of 558.5 ± 3.3 Ma and 338.2 ± 2 Ma, respectively. All obtained values are within uncertainties of the published values. The complete results for samples and standards can be found Tables 1, 2 and 3.

Table 1
U-Pb data table from Zircon determined by LA-ICP-MS for sample QCCMP.

Sample ID	Concentration (ppm)				Radiogenic (corrected) ratio				Calculated age ± σ (Ma)				
QCCMP	U	Th/U	$^{206}Pb/^{204}Pb$	f_{206} (%)	$^{206}Pb/^{238}U$	± 2σ (%)	$^{207}Pb/^{206}Pb$	± 2σ (%)	$^{207}Pb/^{206}Pb$	± 2σ	$^{206}Pb/^{238}U$	± 2σ	Conc (%)
1.sSMPABC107	132.33	0.77	30.83	0.09	0.10431	2.10	0.06230	3.38	684.30	72	639.62	13	106.99
1.sSMPABC108	168.06	0.92	32.87	0.06	0.10511	1.77	0.06140	2.39	653.11	51	644.29	11	101.37
1.sSMPABC109	76.14	0.40	7.70	1.22	0.10437	3.34	0.06163	6.41	661.18	137	639.97	20	103.32
1.sSMPABC110	191.79	1.00	127.30	0.00	0.10682	2.08	0.06102	3.54	639.94	76	654.25	13	97.81
1.sSMPABC111	120.60	0.78	106.90	0.00	0.10683	1.95	0.06193	3.29	671.69	70	654.31	12	102.66
1.sSMPABC112	48.82	0.51	8.69	0.18	0.10442	2.12	0.06225	3.90	682.67	83	640.26	13	106.62
1.sSMPABC113	181.92	0.71	3030.66	0.00	0.10644	1.71	0.06148	2.50	656.07	54	652.04	11	100.62
1.sSMPABC114	389.40	1.38	33.63	0.31	0.10548	1.81	0.06175	2.72	665.63	58	646.44	11	102.97
1.sSMPABC115	607.33	1.87	597.58	0.00	0.10557	1.65	0.06224	2.25	682.37	48	646.97	10	105.47
1.sSMPABC116	93.78	0.95	15.97	0.43	0.10481	2.67	0.06126	5.50	648.27	118	642.54	16	100.89
1.sSMPABC119	198.24	0.69	303.39	0.00	0.10611	2.04	0.06232	3.08	685.11	66	650.12	13	105.38
1.sSMPABC120	186.93	1.18	140.90	1.00	0.10533	2.62	0.06184	4.31	668.67	92	645.57	16	103.58
1.sSMPABC128	175.18	0.81	56.16	0.15	0.10544	1.77	0.06210	2.37	677.55	51	646.21	11	104.85
1.sSMPABC129	238.52	0.99	34.91	1.00	0.10601	2.56	0.06237	4.05	686.66	86	649.53	16	105.72
1.sSMPABC132	150.20	0.74	17.63	0.80	0.10628	2.31	0.06117	3.58	645.11	77	651.11	14	99.08
1.sSMPABC135	131.39	0.54	54.77	1.00	0.10602	2.75	0.06178	4.58	666.52	98	649.59	17	102.61
1.sSMPABC136	157.71	1.15	174.00	0.00	0.10643	1.75	0.06108	2.39	642.05	51	651.98	11	98.48
1.sSMPABC139	138.66	0.74	153.17	0.00	0.10591	1.78	0.06146	2.38	655.37	51	648.95	11	100.99
1.sSMPABC140	232.09	0.85	3899.86	0.00	0.10658	1.75	0.06193	2.36	671.69	50	652.86	11	102.89

f206 is the percentage of common Pb estimated from 204Pb counts.
Concordance in %.

Table 2
U-Pb data table from Zircon determined by LA-ICP-MS for sample QCCMPV.

Sample ID	Concentration (ppm)				Radiogenic (corrected) ratio				Calculated age ± σ (Ma)				
QCCMPV	U	Th/U	$^{206}Pb/^{204}Pb$	f_{206} (%)	$^{206}Pb/^{238}U$	± 2σ (%)	$^{207}Pb/^{206}Pb$	± 2σ (%)	$^{207}Pb/^{206}Pb$	± 2σ	$^{206}Pb/^{238}U$	± 2σ	Conc (%)
1.sSMPABC159	250.58	1.05	59.48	1.00	0.10876	2.60	0.06087	4.07	634.72	88	665.54	16	95.37
1.sSMPABC160	152.14	0.64	85.81	0.08	0.10722	1.82	0.06199	2.40	673.75	51	656.58	11	102.61
1.sSMPABC167	88.56	0.97	1497.34	0.00	0.10911	1.96	0.06087	3.32	634.64	71	667.58	12	95.07
1.sSMPABC168	123.30	1.25	35.46	0.11	0.10773	1.85	0.06187	2.64	669.65	57	659.55	12	101.53
1.sSMPABC170	276.70	1.53	29.90	0.36	0.10792	2.41	0.06136	4.09	651.71	88	660.66	15	98.65
1.sSMPABC171	154.84	0.67	38.46	0.00	0.1076	1.82	0.06166	2.47	662.34	53	658.79	11	100.54
1.sSMPABC172	251.05	1.78	28.07	0.41	0.10804	2.47	0.06098	4.56	638.53	98	661.35	16	96.55
1.sSMPABC173	208.44	0.78	36.58	0.30	0.10841	2.28	0.06104	4.09	640.79	88	663.51	14	96.58
1.sSMPABC174	181.43	0.59	3069.02	0.00	0.10863	2.01	0.06117	2.84	645.22	61	664.79	13	97.06
1.sSMPABC175	173.40	0.82	23.74	0.34	0.1076	2.04	0.06198	3.26	673.30	70	658.79	13	102.20
1.sSMPABC176	54.71	1.02	11.42	0.00	0.108	2.19	0.06149	4.00	656.42	86	661.12	14	99.29
1.sSMPABC177	106.52	0.85	1809.35	0.00	0.10781	2.30	0.06189	3.97	670.31	85	660.02	14	101.56
1.sSMPABC178	99.83	0.81	29.19	0.01	0.1076	1.88	0.06192	2.78	671.43	59	658.79	12	101.92
1.sSMPABC179	143.19	0.94	301.73	0.00	0.10852	1.90	0.06102	3.05	639.94	66	664.15	12	96.36
1.sSMPABC180	140.86	1.07	2381.16	0.00	0.10836	2.33	0.06128	4.24	649.08	91	663.22	15	97.87

f206 is the percentage of common Pb estimated from 204Pb counts.
Concordance in %.

Table 3
U-Pb data table from Zircon determined by LA-ICP-MS for sample QC16′.

Sample ID	Concentration (ppm)				Radiogenic (corrected) ratio				Calculated age ± σ (Ma)				
QC16	U	Th/U	$^{206}Pb/^{204}Pb$	f_{206} (%)	$^{206}Pb/^{238}U$	± 2σ (%)	$^{207}Pb/^{206}Pb$	± 2σ (%)	$^{207}Pb/^{206}Pb$	± 2σ	$^{206}Pb/^{238}U$	± 2σ	Conc (%)
1.sSMPABC067	554.89	0.05	88.56	0.08	0.0991	1.74	0.06064	2.72	626.59	59	609.13	10	102.87
1.sSMPABC068	176.71	0.73	29.53	1.00	0.09869	2.69	0.06087	4.27	634.64	92	606.73	16	104.60
1.sSMPABC069	455.55	0.19	208.79	1.00	0.09765	2.62	0.06105	3.94	641.12	85	600.62	15	106.74
1.sSMPABC070	626.66	0.20	126.83	1.00	0.09892	2.75	0.06093	4.42	636.85	95	608.08	16	104.73
1.sSMPABC072	744.38	0.11	13255.42	0.00	0.09993	1.78	0.06100	2.82	639.23	61	614.00	10	104.11
1.sSMPABC073	348.21	0.24	164.74	0.03	0.10431	1.77	0.06055	2.31	623.31	50	639.62	11	97.45
1.sSMPABC074	103.00	0.69	1718.25	0.00	0.09354	2.39	0.06105	5.14	641.00	111	576.44	13	111.20
1.sSMPABC075	77.18	0.83	1423.37	0.00	0.10449	2.30	0.06042	4.63	618.65	100	640.67	14	96.56
1.sSMPABC076	600.76	0.13	48.02	0.25	0.0912	1.88	0.06121	3.05	646.55	66	562.63	10	114.92
1.sSMPABC077	137.52	0.48	2490.17	0.00	0.10182	2.63	0.06088	5.49	635.00	118	625.07	16	101.59
1.sSMPABC078	72.17	1.30	1303.26	0.00	0.10117	1.84	0.06110	2.78	642.76	60	621.26	11	103.46
1.sSMPABC079	507.21	0.13	29.87	0.37	0.09764	1.92	0.06090	3.48	635.74	75	600.56	11	105.86
1.sSMPABC087	1606.03	0.35	166.46	0.10	0.06952	1.72	0.06124	2.47	647.72	53	433.26	7	149.50
1.sSMPABC089	478.17	0.23	54.93	0.01	0.10471	2.12	0.06046	3.67	620.14	79	641.95	13	96.60
1.sSMPABC090	481.68	0.16	68.05	0.09	0.10435	1.75	0.06071	2.33	629.13	50	639.85	11	98.33
1.sSMPABC091	250.83	0.82	66.20	0.02	0.10414	1.86	0.06073	2.70	629.51	58	638.63	11	98.57
1.sSMPABC094	312.35	0.30	5769.82	0.00	0.10426	1.98	0.06065	3.53	626.84	76	639.33	12	98.05
1.sSMPABC096	718.35	0.06	60.43	0.15	0.09950	1.85	0.06049	2.66	621.21	57	611.48	11	101.59
1.sSMPABC097	64.54	1.77	13.68	1.12	0.10160	2.98	0.05999	5.02	603.28	109	623.78	18	96.71
1.sSMPABC098	189.01	0.42	108.98	0.00	0.10417	1.73	0.06063	2.47	626.13	53	638.80	11	98.02
1.sSMPABC099	256.58	1.06	43.39	0.26	0.10462	1.96	0.06031	3.33	614.73	72	641.43	12	95.84
1.sSMPABC100	599.25	0.11	11051.73	0.00	0.10442	2.11	0.06046	3.37	620.08	73	640.26	13	96.85

f206 is the percentage of common Pb estimated from 204Pb counts.
Concordance in %.

4. Microstructures, crystallographic fabrics and geochronology

4.1. Microstructural observations

The nine selected samples of mylonites from the 4°50′ shear zone have been studied under the optical microscope then EBSD measurements have been performed. Three representative EBSD phase maps sections are displayed in Fig. 7b and c, 8a and 9a. Phase maps of all the samples are available in the supplementary material (Fig. S01 and S02). These samples contain fine to rather coarse grains and display microstructures typical of ductile deformation. Almost all thin sections (except Amd04 in Fig. S01) show alternating layers of alkali feldspar, plagioclase, and quartz (Fig. 7b, Fig. 8a, Fig. 10a, and Fig. S02). Some samples locally show lepidoblastic layers containing principally muscovite, amphibole, and titanite. This layering marks the ~ NS-trending foliation. In several samples with various quartz contains, quartz layers locally curve and crosscut feldspar layers. In addition, in some samples, quartz forms anastomosed layers suggesting that it crystallized from a fluid infiltrating a rock in which alkali feldspar and plagioclase were already in the solid-state (Fig. 9a and b).

Samples from the southern segment exhibit mono-mineralic layers of Kfs, plagioclase, and quartz (Fig. 7b and c, Fig. 9a and Fig. 10a); those from the northern domain show relatively thinner quartz layers (*e.g.,* Amd02 in Fig. S01) but still parallel to the mylonitic foliation.

In most cases, crystals in the different layers exhibit an elongate shape parallel to the macroscopic lineation (North trending; *e.g.,* Fig. 7a). However, in several samples (*e.g.,* QC2; Qc13; Qc17; Qccmp), grains in quartz layers parallel to the foliation display an elongation oblique to the layering (~30°; Fig. 6b, Fig. 7a, and Fig. 8a and b) and form a second foliation suggesting a sinistral shearing dominantly localized in these quartz ribbons. The quartz grains size varies from 30 μm to ~1.8 mm. Fine-grained quartz is scattered in the stiffer Kfs and plagioclase layers, where it usually displays an interstitial habitus, while medium/large size grains occur mainly in monomineralic layers (Fig. 4c). These interstitial grains are filling microcracks in plagioclase and small rounded grains of quartz are also observed inside large feldspar grains (Fig. 4a, b and c, and Fig. 5b). Most interstitial grains (at the boundaries or inside the feldspar) display the same extinction and, thus, share the same orientation than quartz in the layers. The grains inside the ribbons form sub-elliptical grains with curly boundaries and some display subgrains and undulose extinctions (Fig. 5e, Fig. 6b, and c). The subgrains boundaries are perpendicular to oblique to the grains elongations (Fig. 5e). Some quartz grains display a tendency to be polyhedral with straight/rounded boundaries (Fig. 5c) where they frequently show undulose extinction and subgrains boundaries parallel/oblique to the grains elongation supporting that they underwent plastic deformation (Fig. 5c).

Thus, intracrystalline deformation features are observed in small grains as well as larger ones. A slight misorientation affects almost all quartz grains.

Kfs and plagioclase share most microstructural characteristics. They are concentrated in layers parallel to the mylonitic foliation, and their size is varying from ~ 20 μm to ~1.5 mm. Both K-feldspar and plagioclase display undulose extinction (Fig. 5a and b) and are corroded, with quartz grains crystallized in embayments (Fig. 4c and Fig. 4d). Feldspar porphyroclasts display asymmetric tails consistent with dextral shear sense (*e.g.,* Fig. 3a and b). The Kfs seem to be more deformed than the plagioclase. Mechanical twinning and undulose extinction are more frequent in Kfs (Fig. 5a and b) than in plagioclase. However, plagioclase is almost totally altered, which is not the case for the Kfs, and this might bias the comparison. Fig. 7b shows an example of partially recrystallized plagioclase porphyroclast from sample QC2, characterized by corroded boundaries and embayments filled by fine-grained K-feldspar. K-feldspar is also filling the micro-cracks within the plagioclase. In the same sample, some Kfs porphyroclasts are bounded by fine-grained plagioclase (Fig. 7c) that may infill small boundary embayments and fractures inside

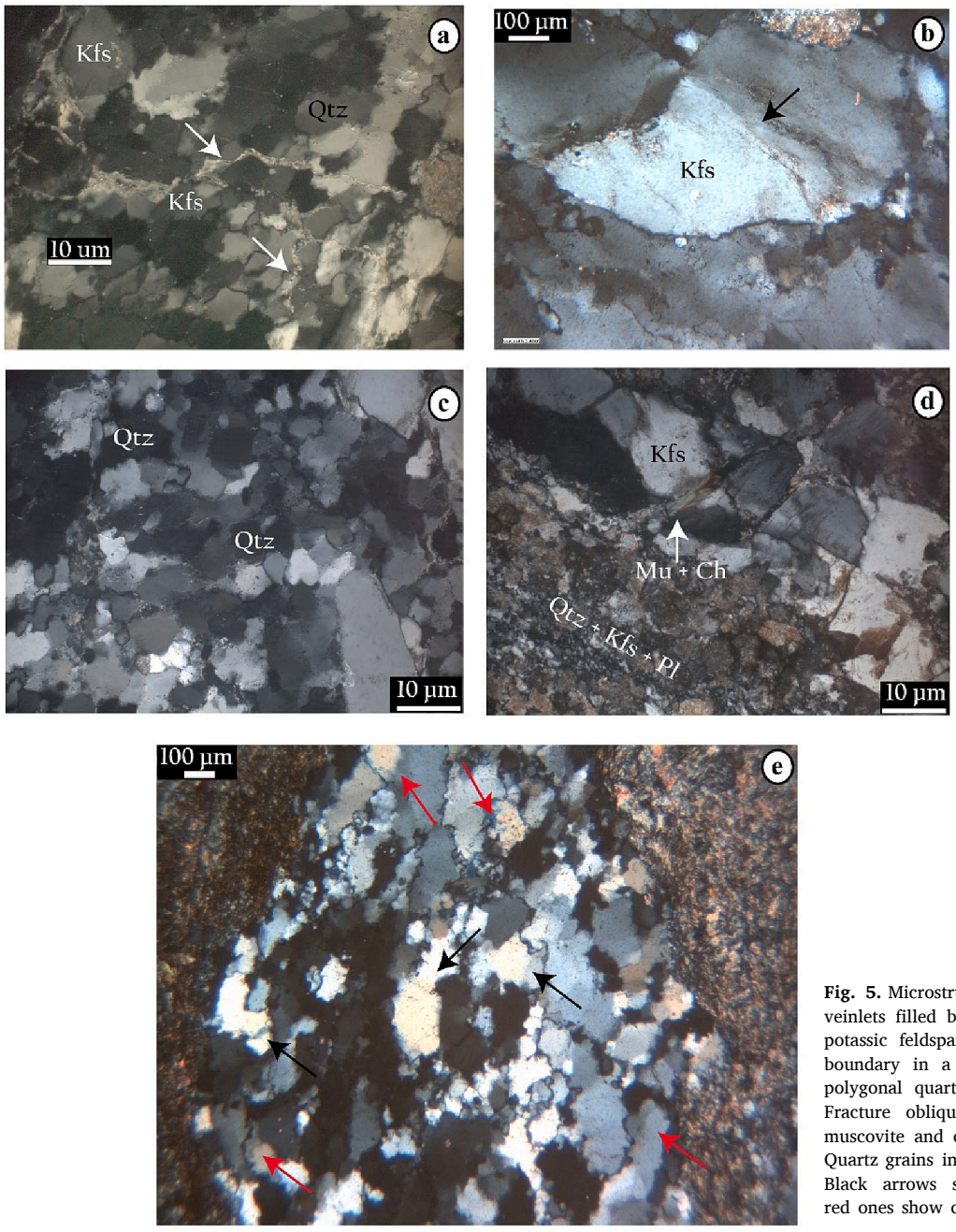

Fig. 5. Microstructures of studied sam-ples 2: a. irregular veinlets filled by micas along the boundaries of the potassic feldspar grains (white arrows). b. Sub-grain boundary in a potassic feldspar porphyroclast. c. Sub-polygonal quartz grains surrounding the feldspar grains. d. Fracture oblique to the mylonitic foliation filled by muscovite and chlorite between large feldspar grains. e. Quartz grains in ribbon parallel to the mylonitic foliation. Black arrows show straight subgrain boundaries while red ones show curved subgrain boundaries.

the K-feldspar. In both cases, these feldspar grains are also surrounded by small quartz grains (Fig. 7b and c).

Amphibole, small to medium in size, is present in two samples (QC17, Qccmp). They are dominantly embedded between the feldspar grains but, in QC17, they form monomineralic aggregates parallel to the foliation, frequently associated to quartz ribbons, even when those crosscut the foliation (Fig. 9). In both samples, amphibole crystals are elongated parallel to the lineation (Fig. 9a and b).

Micas and some chlorites are in small proportion in the studied rocks. They are frequently observed in micro-cracks (Fig. 5a) and do not show any microstructural fabric. Amphibole is present in two samples (QC17 = 21%; QCCMP = 0.4%). This supports that the deformation occurred under amphibolite facies conditions, and that retrogression to the greenschist facies happened after the deformation.

4.2. *Crystallographic preferred orientation*

The crystallographic preferred orientation of the main phases of the nine selected samples has been measured using the EBSD technique (Fig. S03, S04, and S05 are in supplementary material).

For all selected samples the quartz CPO displays an axial symmetry (Fig. 6d, Fig. 8c, Fig. 9c, and Fig. 10), with a strong concentration of [0001] (up to > 6 MUD) close to the Y structural axis, which is perpendicular to the thin section (Fig. 10). The a$(11\bar{2}0)$ and m$(10\bar{1}0)$ poles are dispersed in a girdle around [0001] with, for some samples, a weak maximum of the a-axis ~ parallel to the foliation.

There is no significant difference between the CPO of the quartz grains dispersed in feldspar layers and those in the quartz layers, even where the layer escapes from the foliation and crosscuts it (Fig. 6d, Fig. 8c and Fig. 9c). These CPO therefore substantiate that, the quartz C-axis are dominantly sub-vertical to vertical, parallel to the foliation and

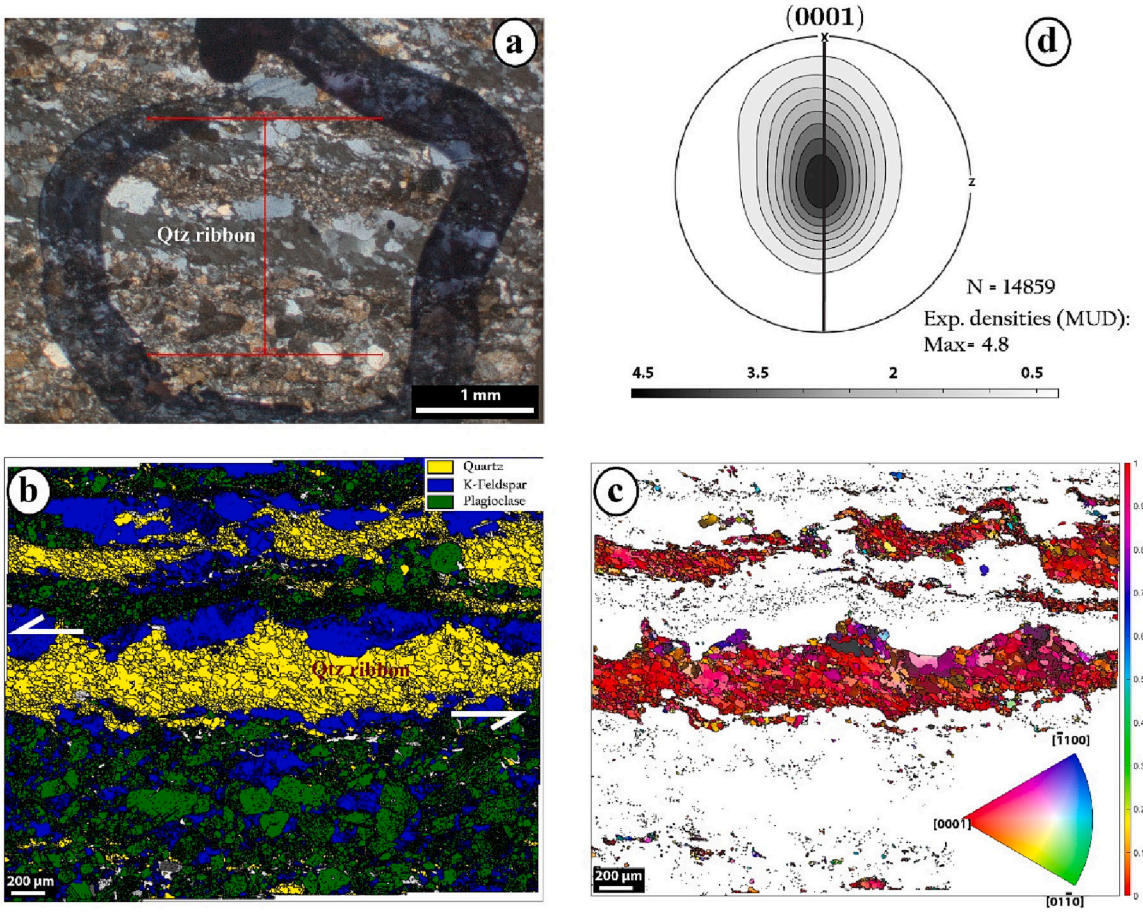

Fig. 6. Quartz ribbon orientation and CPO in sample QC16′a. Quartz ribbon in the thin section. b. EBSD phase map showing the quartz ribbons, the large K-feldspar and plagioclase grains. The quartz grain elongation suggests a sinistral shear sense. c. Orientation map of the quartz grains coloured depending on the crystallographic direction (coloured by inverse pole figure orientation map) parallel to the Y structural axis (perpendicular to the thin section). This map shows that a large majority of grain is oriented with [0001] parallel or close to the Y structural axis. d. Preferred orientation of quartz [0001] that also displays a concentration centered on the Y axis.

normal to the lineation. This agrees with the dominant prism-<a> slip system (*e.g.,* Stipp et al., 2002) for quartz in all samples.

Plagioclase has weak, but usually well-defined CPO. It displays a maximum concentration of the [1 0 0] axis near the lineation (X-axis direction) and a maximum of (0 0 1) perpendicular to the foliation (Z-axis direction; Fig. 11). There is no significant difference between the CPO of the porphyroclasts and of the finer grains. The CPO of K-feldspar is less clearly defined, especially for sample Qccmp; it is characterized by a maximum of [1 0 0] axis parallel to the X-axis direction (Fig. 11) and (0 1 0) plane parallel to the XZ plane. Coarser and finer Kfs grains display similar CPO.

The amphibole has a well-defined and rather strong crystallographic fabric. The CPO displays a maximum value > 6 MUD and is characterized by a point maximum of [0 0 1] close to the X-structural axis (Fig. 11) and a concentration of (1 0 0) poles close to the Z direction. There is a good correlation between the amphibole CPO and the plagioclase. Maximum concentrations of [0 0 1] and (1 0 0) of amphibole are respectively correlated with those of [1 0 0] and (0 0 1) of plagioclase. In addition, quartz [0001] strong concentration is correlated with the [0 1 0] of amphibole.

4.3. Geochronology

Three samples were dated, the QCCMP and QC16 granitoids and the QCCMPV, which is a xenolith in QCCMP (Figs. 12, 13, and 14 respectively).

QCCMP and QCCMPV samples display euhedral elongated zircon crystals of medium size (100–200 µm), typical of magmatic rocks. In the QCCMP sample (Fig. 12), 15 points were analyzed showing a concordant age of 649 ± 3 Ma (MSWD of concordance MSWDc = 1.9) and a discordia age including all points (28 analysis) of 647 ± 3 Ma (MSWDc = 0.79). The Th/U ratio is between 0.4 and 1.8 with an average of 0.88.

In sample QCCMPV, 28 points were analyzed of which 23 gave a concordant age of 661 ± 3 Ma (MSWDc = 0.26; Fig. 14). Their Th/U ratio is between 0.51 and 1.78. The magmatic-like crystals may show thin recrystallized rims brighter than the cores. Such a thicker rim could be analyzed. It corresponds to bright recrystallized rim. It provides a younger concordant point giving an age of 617 ± 18 Ma (Th/U – 0.21).

QC16′ sample display euhedral to subhedral zircon crystals of variable size (50–200 µm). 28 points were analyzed of which 9 gave a concordant age of 639 ± 4 Ma (MSWDc = 2.1 and Th/U ratio between 0.11 and 1.06), 3 points give a concordant age of 623 ± 8 Ma (MSWDc = 0.2 and highest Th/U ratio, between 0.8 and 1.78) and 7 points giving a concordant age of 609 ± 4 Ma ((MSWD = 3.). six of the seven analyses have low Th/U, between 0.05 and 0.2 (Fig. 13).

5. Discussion

The 4°50 SZ is one of the pluri-kilometers wide shear zone already described through the world and that likely were lithospheric, as suggested by geophysical data (*e.g.,* Good and De Wit 1997; Vauchez and Tommasi, 2003; Vauchez et al., 2012). These major shear zones were

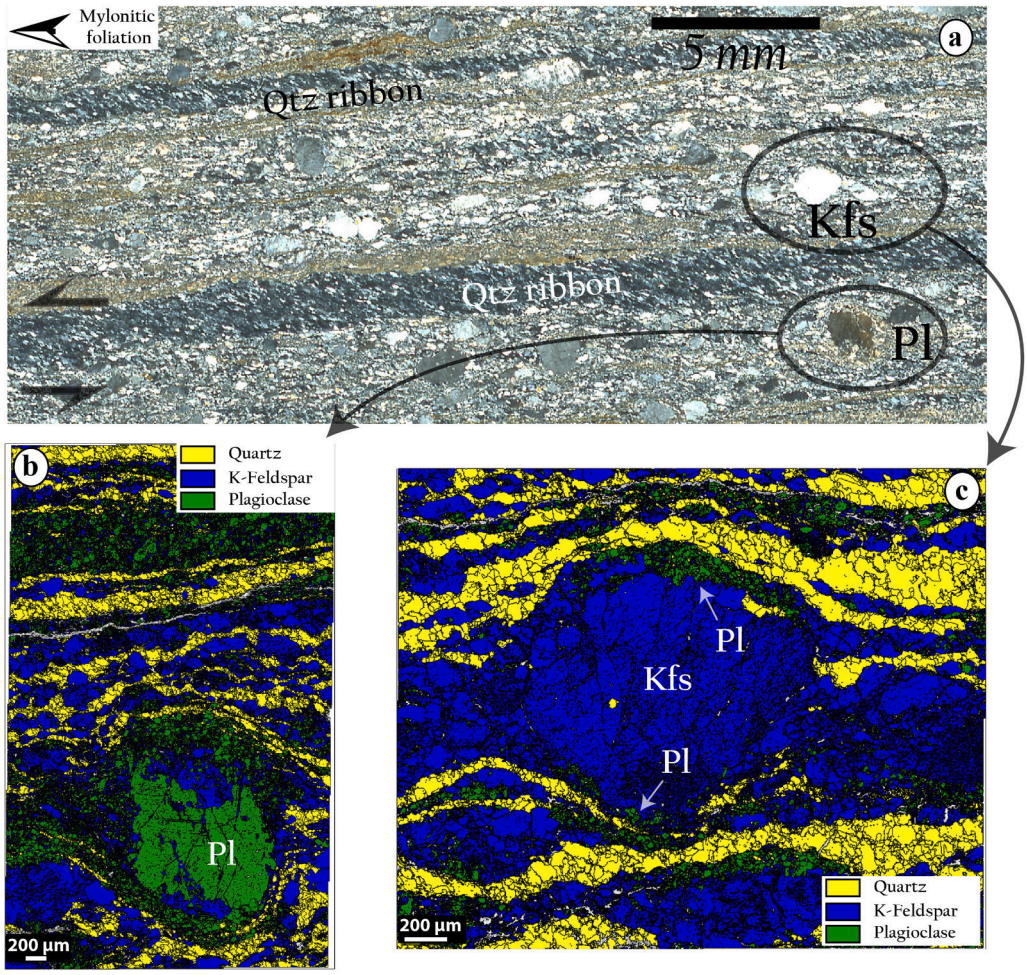

Fig. 7. Replacement reactions between feldspar in sample QC2: a. location of the feldspar porphyroclasts in the thin section and location of the quartz ribbons. b. EBSD phase map of a plagioclase, porphyroclast corroded and partially replaced by K-feldspar. c. EBSD phase map showing the Kfs porphyroclast around which fine-grained plagioclase fill embayment and small fractures.

active over long period of times and, in most cases, the mylonites formed during the peak activity display evidence of magma-rocks reactions due to the emplacement of *syn*-kinematic plutonic rocks.

5.1. *Deformation mechanism*

The studied mylonites result from the deformation of granitoids and show evidence of ductile deformation at the outcrop scale (Fig. 3) suggesting high-strain dextral shearing (*e.g.,* asymmetric tails on feldspar porphyroclasts; Fig. 3a and b). Dominant feldspathic layers and narrower quartz ones define the ~ NS vertical foliation of the 4°50′ shear zone. At the microscopic scale, they show typical magmatic microstructures associated, in most cases, with alternating monomineralic layers of K-feldspar, plagioclase, and quartz. Crystals in these layers display evidence of moderate to strong intracrystalline solid-state deformation: undulose extinction, local recrystallization, and also fractures filled mainly by quartz (Fig. 4a, b, Fig. 5a and b). In addition, feldspar, in most cases, display a crystallographic fabric: Kfs usually show a CPO (Fig. 11) supporting dislocation-creep with the activation of the [100] (010) slip system (*e.g.,* Chen et al., 2021 and references therein), and plagioclase display a fabric characteristic of the activation of the [100] (001) slip system (*e.g.,* Montardi and Mainprice, 1987; Stünitz et al., 2003). The development of such feldspar CPO is considered as due to submagmatic shearing (*e.g.,* Bouchez et al., 1992; Tommasi et al., 1994; Hasalová et al., 2008). Indeed, another important observation is the partial replacement of the plagioclase by the Kfs and, to a lesser extent, the reverse (Fig. 7b and c). These reactions suggest a deformation assisted by percolation of fluids of variable composition (Fig. 7b). This is supported by the crystallization of oblique quartz ribbons after formation of the feldspathic layers, the corrosion of plagioclases and, in a lesser extent, of Kfs and the filling of embayments by Kfs and plagioclase respectively.

Quartz occurs in monomineralic layers parallel to the feldspathic ones, but, locally these quartz layers curve and form irregular veins crosscutting the mylonitic foliation marked by feldspar and, when present, by amphibole layers (Fig. 9a). In addition, the crystallographic fabric of quartz in the crosscutting veins and in the layers parallel to the foliation is similar (Fig. 8c and 9). In all cases, the quartz CPO is characterized by a strong concentration of [0001] parallel to the foliation plane and orthogonal to the lineation (Y structural axis). This is for instance the case in samples Qc13 (Fig. 8c and Fig. 10) and in Qc17 (Fig. 9c and 11) in which quartz layers display similar CPO independently of their orientation relative to the foliation. In several samples, the quartz grains in the ribbons display evidence of dislocation creep and the largest ones have an elongate shape oblique to the layering. On the other hand, the interstitial habitus of quartz grains dispersed in feldspathic layers and the shape of quartz veins cross-cutting the foliation have been preserved. This likely indicates that a moderate sinistral shear strain, subsequent to the formation of the quartz layers, was localized in the weakest parts of the rock, *i.e.,* the quartz ribbons (Fig. 6b, 7a and 8b), and was accommodated through dislocations creep. Furthermore, the quartz filling fractures in feldspar is in continuity with

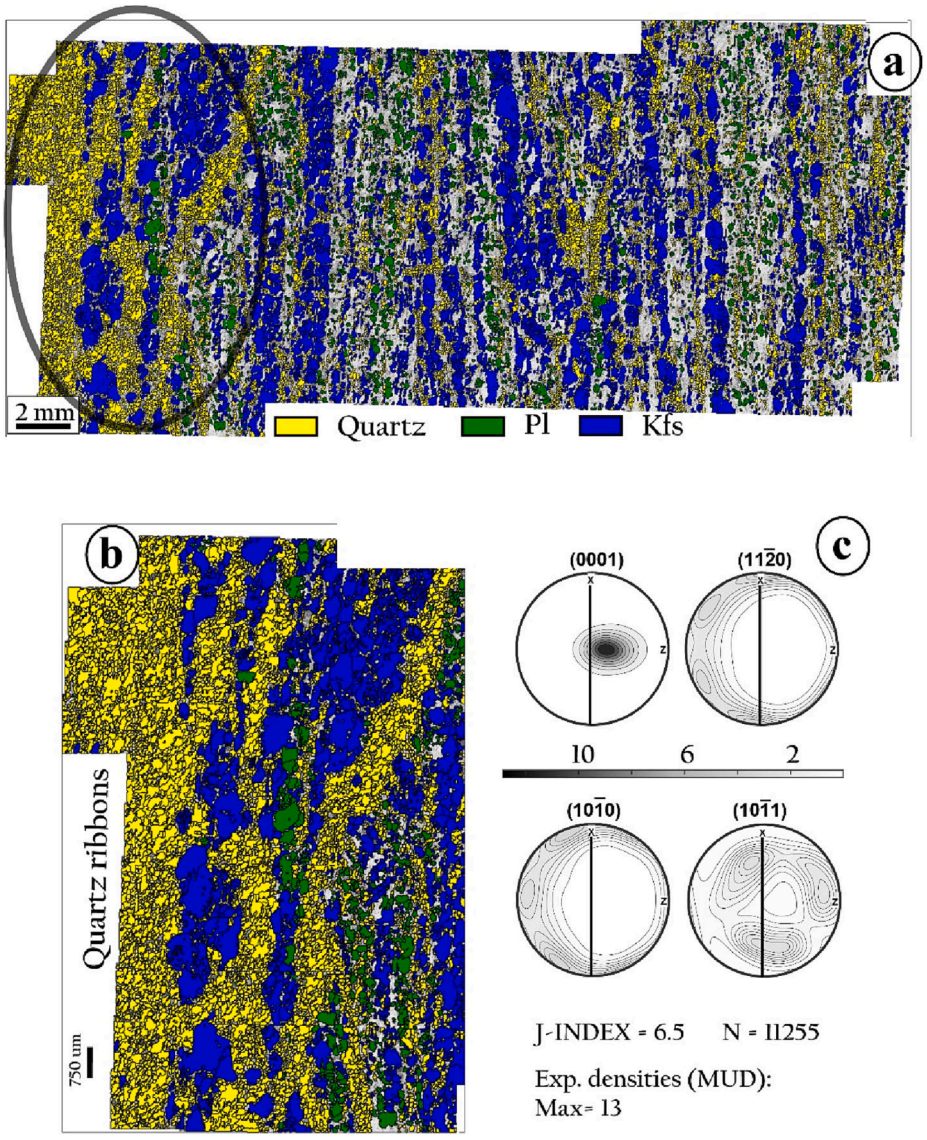

Fig. 8. Mono-layering of minerals constituting the QC13 thin section with quartz ribbons. a. Localization of the Quartz ribbons in the thin section. b. EBSD phase map of the sample QC13 showing the quartz ribbons with some segments oblique on the foliation. c. Quartz crystallographic preferred orientation of the quartz ribbons in this section.

large quartz grains neighboring feldspar, supporting that these fractures were initiated in the submagmatic stage (Fig. 4a and b). Altogether these observations suggest that the quartz crystallized (at least partially) from a fluid that percolated the rock, principally along the already present feldspathic layers, but locally through the mylonitic foliation. The crystallographic fabric of quartz likely results from both oriented crystallization and limited solid-state deformation. This points to *syn*-kinematic fluid circulation through magmatic rocks that were already foliated. The activation of the prismatic slip system in the < a > direction is consistent with dislocation creep under relatively high-temperature during magma cooling.

Therefore, quartz and feldspar microstructures and textures consistently show that reactions with a magmatic fluid and a solid-state deformation have been associated. The magmas at the origin of the mylonites parent-rock were likely intruded during the shear deformation within the 4°50′E shear zone. Feldspar crystallized first in Kfs and plagioclase-rich layers and then the quartz. It is also possible that several batches of magma were injected in the magma bodies during a late episode, triggering reactions between already crystallized minerals and the percolating magma. This might have occurred during the early stage of deformation of the 4°50′E shear zone. Later on, after crystallization of quartz but still under relatively high temperature, a moderate solid-state deformation, mostly localized in the weakest part of the rocks (*i.e.*, quartz ribbons), accommodated sinistral shearing. This points to superposition of several stages of mylonites deformation within the 4°50′E shear zone. Altogether, these observations support a scenario in which:

Felsic magmas, mostly granitoids have been intruded in the already active 4°50′ SZ dextral shear zone,

Feldspar crystallized first and formed segregated K-feldspar- and plagioclase-rich layers,

A solid-state deformation of variable intensity affected the feldspars, which are largely recrystallized in some samples and much less in other ones. However, the layered structure was preserved,

Fluid continue percolating along these layers during deformation, crystallizing quartz ribbons,

Several fluid batches percolated the mylonites, triggering fluid-rock reactions that affected plagioclase and K-feldspar. These fluids might result from migmatization of surrounding, less refractory rocks.

Still under relatively high temperature, a moderate sinistral shear reactivation occurred and this deformation was mostly localized in

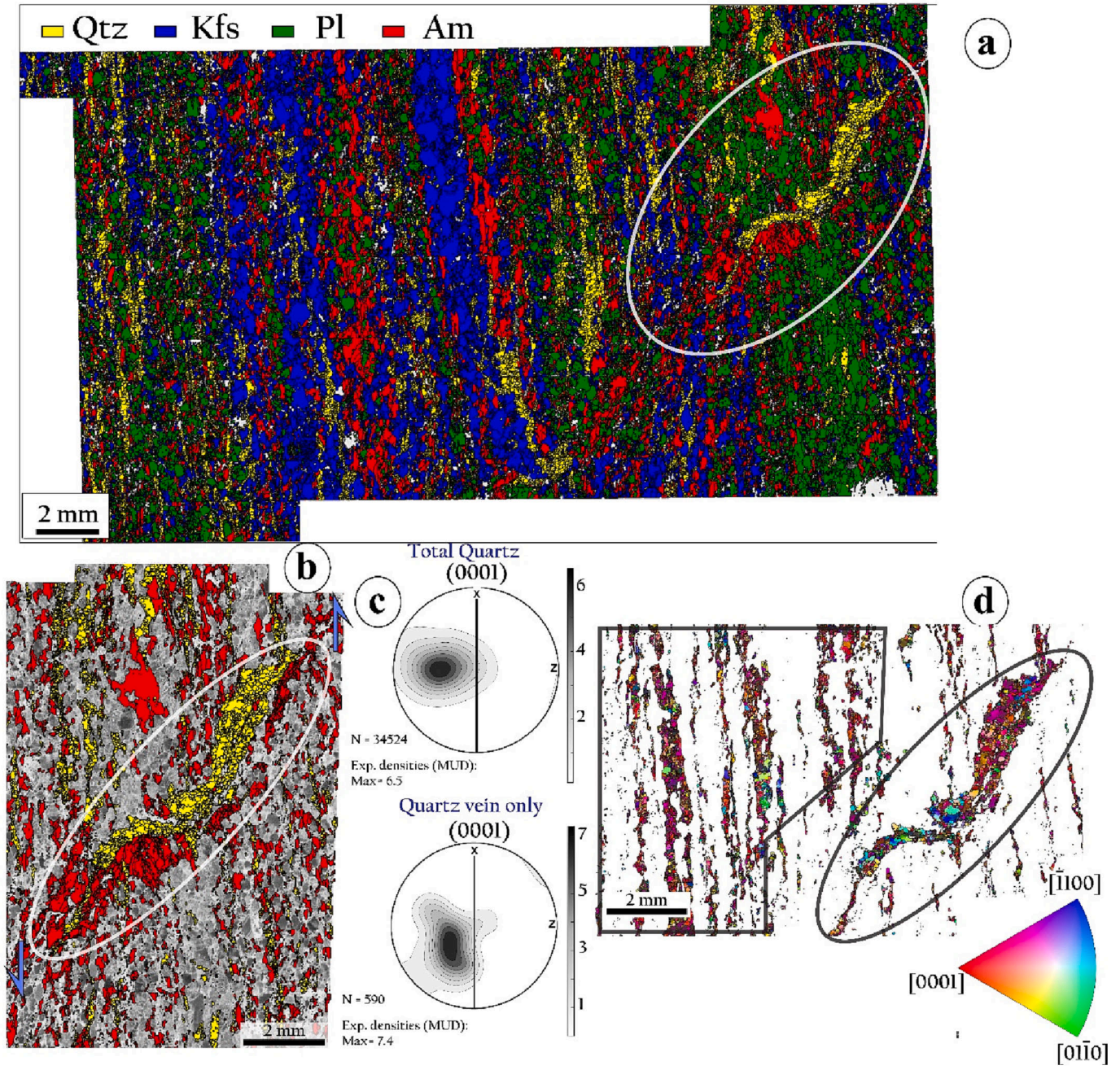

Fig. 9. Quartz vein oblique to the primary mylonitic foliation. a. EBSD phase map of the entire QC17 sample. b. Zoom on the quartz oblique vein associated to amphibole croscutting the foliation. c. Crystallographic preferred orientation comparison between quartz in all the thin section and those in the crosscutting vein. d. Orientation map coloured depending on the crystallographic direction of quartz grains parallel to the Y structural axis (perpendicular to the thin section). It clearly shows that the orientation of quartz grains in the vein (in the ellipse) is similar to the orientation of quartz grains in the layers parallel to the mylonitic foliation outside the oblique vein.

quartz layers.

5.2. Successive dextral-sinistral shearing through time

Although several reactivations of the 4°50′ SZ have been reported by previous studies (see the Geological Setting section for references), initial ductile deformations and, thus, its kinematic evolution are still poorly characterized. This is, therefore, limiting the understanding of the geodynamic role of this shear zone and its continuation to the South (Kandi- and Transbrasiliano SZ) during Western Gondwana building. From our new results, we can substantiate the following evolution:

5.2.1. Initial dextral episode

Mylonites from the 4°50′ SZ share the same microstructures and CPO, *i.e.,* a mylonitic foliation with magmatic texture, marked mainly by Kfs-rich and plagioclase-rich layers locally crossed by oblique quartz-rich ribbons/veins. Phases segregation and shear sense criteria present in several samples support that the magmatic bodies emplaced in the 4°50′ SZ have underwent the same deformation stages, especially an initial dextral transcurrent one that occurred during the crystallization of feldspar, leading to phases segregation. This deformation likely continued in the solid-state stage contemporaneously with the percolation of magmatic fluids of variable composition. Considering the microstructure and the geochronological data obtained in this study, we

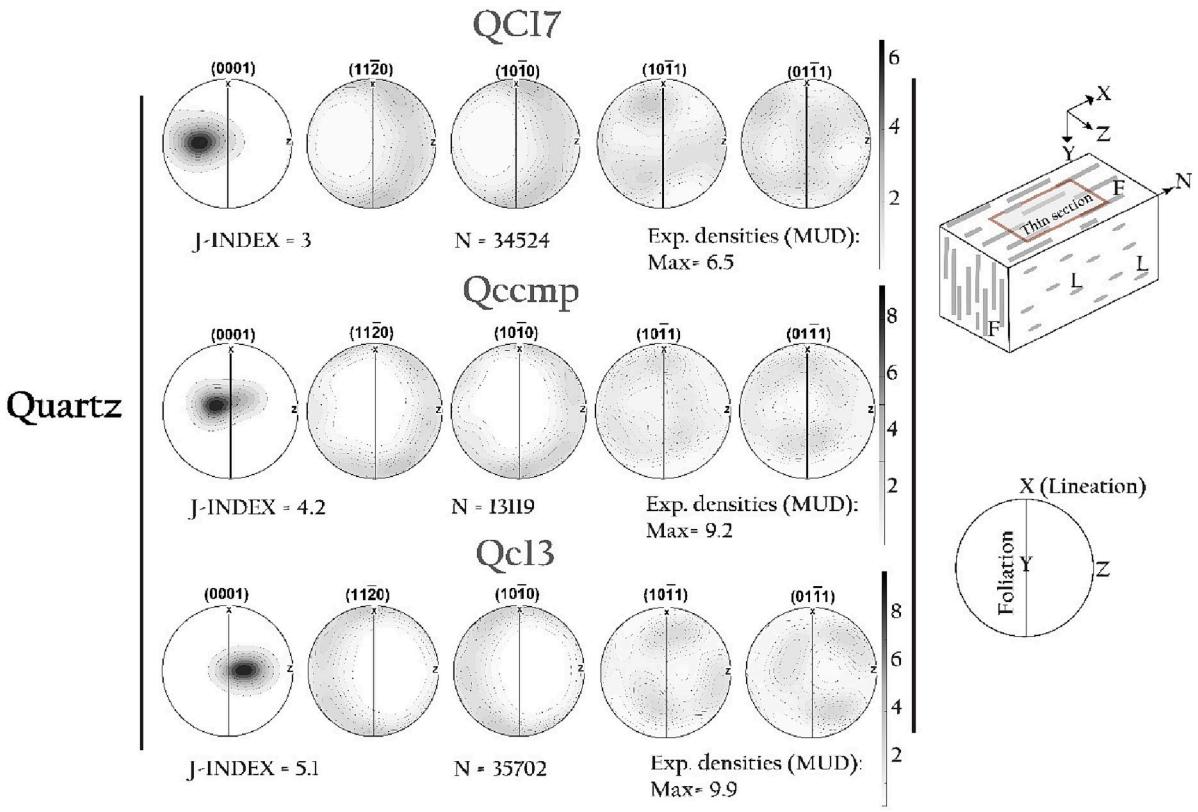

Fig. 10. Quartz crystallographic preferred orientation for three representative samples (Qc13, Qc17 and Qccmp). Thin sections were cut parallel to the XZ structural plane (X parallel to the stretching lineation and Z orthogonal to the foliation plane). The mean orientation of each grain was plotted (one point per grain). Cartoons on the right illustrate how thin sections were cut and the orientation of the CPO plot in the structural referential.

suggest a scenario with a major initial dextral episode that occurred during the intrusion of consecutive granitoids in the shear zone (661 ± 3 Ma, 649 ± 3 Ma, and 639 ± 2 Ma) and after their solidification, and perhaps until the most recent obtained ages (623 ± 4 Ma and 609 ± 2 Ma). This supports a protracted dextral activity of the 4°50′ SZ over>20 My.

5.2.2. *Sinistral local reactivation*

As mentioned above, quartz ribbons in several samples display evidence of a moderate solid-state sinistral shear strain. This deformation is younger than the ages obtained for the dextral episode, but it occurred under relatively high-temperature thus probably soon after the crystallization of quartz. However, it remains difficult yet to determine an age for this sinistral episode in the 4°50′ SZ.

5.3. *Nature and ages of the protolith and relationship with the adjacent terranes*

The geochronological data suggest that the granitoid protoliths of studied mylonites from the 4°50′ SZ intruded the crust at 661 ± 3 Ma, 649 ± 3 Ma, and 639 ± 2 Ma. In addition, the geochronological data show that some concordant analyzes exhibit an age of 623 ± 4 Ma and 609 ± 2 Ma. These ages (623 ± 4 Ma and 609 ± 2 Ma) are concordant with those of the high-temperature granulitic metamorphism (850 °C; 0.8–0.7 GPa, 700 °C; 0.4–0.3 GPa respectively) known in LATEA (Bertrand et al., 1986; Barbey et al., 1989; Bendaoud et al., 2004; Bendaoud et al., 2008; Fettous, 2016). Older ages obtained on the 4°50′E correspond to geodynamic events already documented in the Hoggar: 661 ± 2.8 and 649 ± 2.9 Ma ages correspond mainly to those considered for the subduction (Caby, 2003; Benmerzoug, 2012). And 639 ± 2 Ma is similar to the age of the Eheli batholith in the Aouilène terrane (638 ± 5 Ma; Benmerzoug-Béchiri, 2012), regarded as the latest *syn*-subduction granite known so far.

Subduction ages close to those obtained in this study have also been reported for the Laouni terrane (East of the 4°50′ SZ, Fig. 2a). Neoproterozoic inherited zircon (640 Ma) of the Tin Begane batholith (Bettioui et al., 2022) and ages of 640 Ma obtained in the southern part of Laouni (Bowden et al., 2014) might indicate that this terrane shares the same tectonic behavior than the Aouilène terrane, and then show a similar active margin character, as described by Deramchi et al., (2020) and Ouadahi et al., (2022). These similarities in age suggest that emplacement of the granitoid protoliths of the 4°50′ SZ mylonites occurred during the subduction and thus that the shear zone was already active.

In addition, a migmatization event has been documented in the LATEA microcontinent from 630 Ma to ~ 577 ± 22 Ma (Bouzeguella-Talmat, 2014; Liégeois et al., 2003) and several migmatitic rocks are neighboring the 4°50′ SZ. Accordingly, the most recent ages obtained for our samples are contemporaneous with those of the migmatites known so far in the neighboring terranes.

5.4. *Tectonic movements, obtained ages, and deformation relationship:*

It is therefore important to underlie the relationship between the tectonic movements and the mylonites evolution in the 4°50′ SZ. The geochronological data provide several ages ranging from 661 ± 3 Ma to 609 ± 2 Ma. It has been noted in the previous section that the protoliths of the studied mylonites intruded the crust successively from 661 ± 3 Ma to 639 ± 2 Ma. Their microstructure suggest that they have been deformed during their crystallization, at least for the Kfs and the plagioclase during submagmatic stage, and continued after being crystallized. Thereafter, they have been affected by a migmatization between 623 ± 4 Ma and 609 ± 2 Ma that is widely known in the neighboring areas (Bendaoud et al., 2008; Bowden et al., 2014; Fettous,

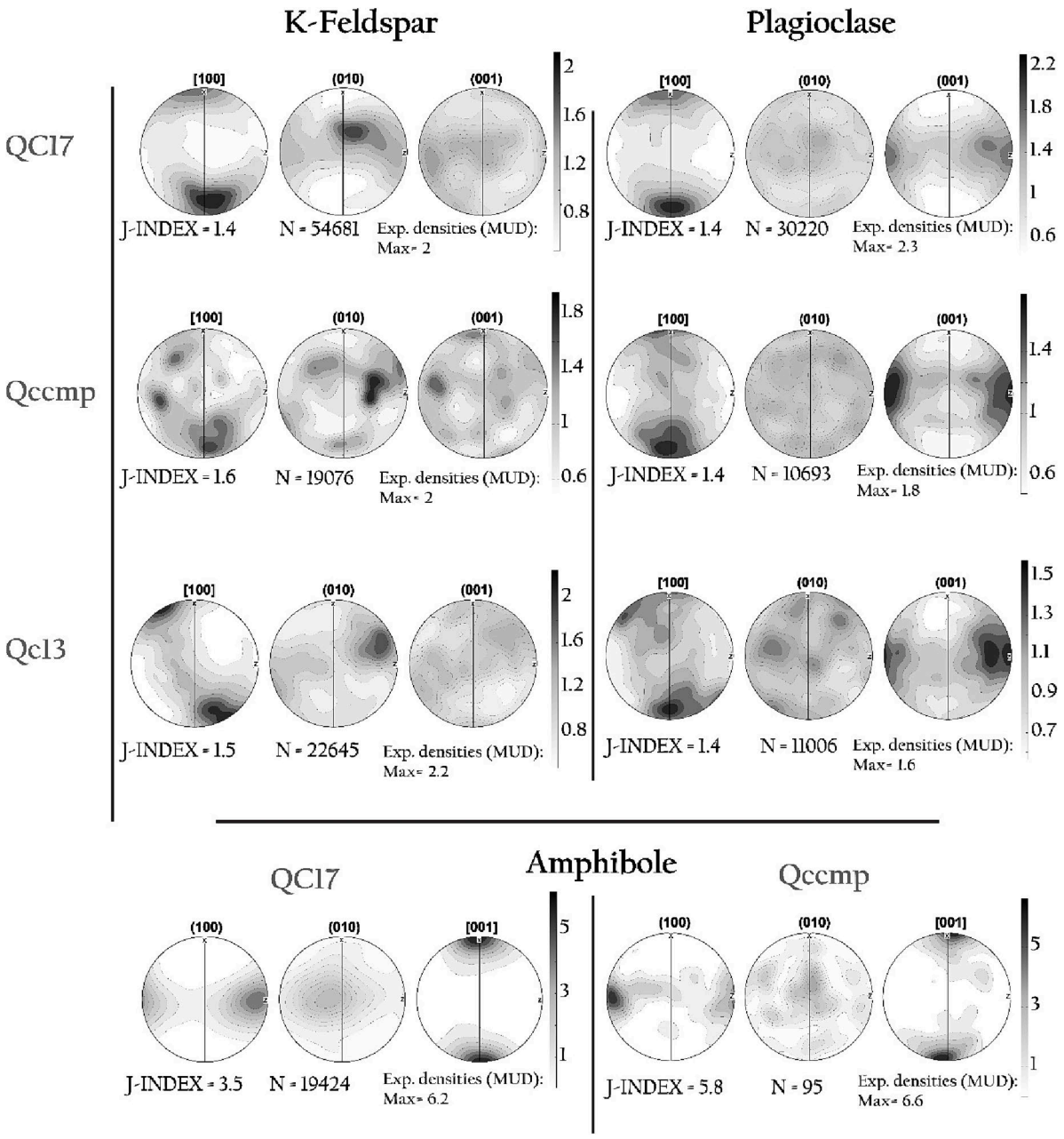

Fig. 11. Crystallographic preferred orientation of K-feldspar and plagioclase for samples Qc13, Qc17 and Qccmp, and of amphibole for two of them (Qc17 and Qccmp).

2016; Fettous et al., 2018; Bettioui et al., 2022), and which might be at the origin of several magma batches that percolated through the already foliated rocks. The initial dextral tectonic movement likely triggered the formation of these mylonites from 661 ± 3 Ma to 609 ± 2 Ma. This deformation began at least at the submagmatic stage and continues until the solid-state stage. A sinistral reactivation at medium/high temperature that occurred probably after 609 ± 2 Ma affected locally these mylonites. This dextral and sinistral evolution share similarities with the evolution of the Ounane shear zone that bounds LATEA eastward (Fig. 2a). Indeed, the magnetic fabric of the Ounane calc-alkaline granitoid investigated using the Anisotropy of Magnetic Susceptibility (AMS) points to a submagmatic dextral deformation in the Ounane Shear zone at 629 ± 6 Ma followed by a sinistral reactivation that affected a circular granitoid (similar to Taourirt) emplaced at 572 ± 5 Ma (Henry et al., 2018; Nouar et al., 2021).

5.5. Metamorphism grades associated to deformation in the 4°50′ shear zone

The stretching lineation is well defined by the amphibole (Fig. 11) due to the high concentration of its [0 0 1] axis around the horizontal X-structural axis (Fig. 11). Amphibole show a strong CPO supporting that the deformation occurred at relatively high temperature under the amphibolite facies. In addition, feldspars show partial replacement of the plagioclase by the Kfs and the reverse. This metamorphic reaction is typical of fluid percolation, and, thus, suggests that the deformation was assisted by fluid percolation.

This obviously agree with the ages provided by the geochronological data so far (Bendaoud et al., 2008; Bowden et al., 2014, Bettioui et al., 2022, and reference therein), during which a regional migmatization occurred especially in this part of LATEA (*e.g.,* Tidjenouine, Tin Begane, Tamanrasset…). This has been also attested by the presence of crustal

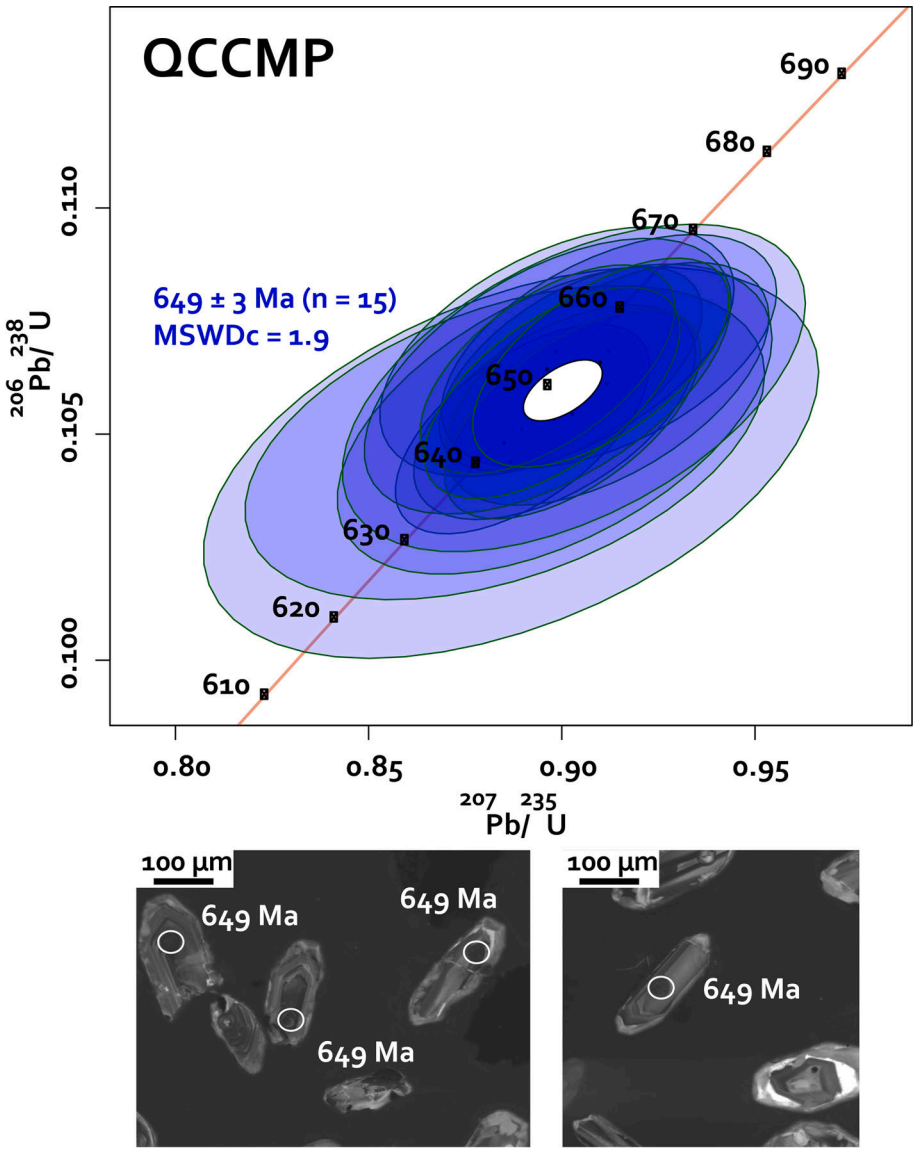

Fig. 12. U-Pb zircon concordia diagram showing the obtained ages for the QCCMP sample with some representative spotted zircon. Top: Coloured ellipses correspond to the different obtained ages of the main zircon crystals. Bottom: SEM images showing the texture of the dated zircon. The white circles indicate the spot analyses localization and the displayed ages are indicating concordia ages.

granitoids with same ages (*e.g.,* Amsel and Tin Begane batholiths; Bouzeguella-Talmat, 2014 and Bettioui et al., 2022 respectively). The sinistral reactivation recorded mainly in quartz ribbons occurred after its crystallization, and probably during the retrogression from the amphibolitic to the greenschist facies.

5.6. *Geodynamical implications*

Geochronological and microstructural results support that granitoids, at the origin of the studied mylonites have been emplaced in the already active 4°50′ SZ. The ages of emplacement are consistent with those considered for *syn*-subduction magmatism in Hoggar (Bechiri-Benmerzoug, 2012) and this supports that the 4°50′ SZ was already active during subduction. In addition, our results validate that mylonites from the 4°50′ SZ have recorded a Pan-African dextral transcurrent deformation that occurred during their emplacement. Two different evolutions are possible after the emplacement of the protoliths:

- The active deformation during the emplacement of the magmatic protoliths continues after crystallization of the feldspathic layers, in association with the percolation of several batches of magmatic fluids along these layers. The percolation of magma batches might continue to a later migmatization episode corresponding to the youngest ages obtained for our samples (623 ± 4 Ma to 609 ± 2 Ma).

- The deformation that occurred after solidification of the feldspar layers may have been synchronous with the later migmatization.

Considering the consistence of the obtained ages in this study with those already obtained for a migmatization episode in neighboring domains, we favor the first scenario.

This main deformation episode was followed by a moderate sinistral ductile shearing under medium/high-temperature conditions. Whatever the scenario, mylonites from the 4°50′ SZ indicate that this shear zone was already active during the subduction stage and continued during the collisional and the post-collisional period.

6. Conclusions

The 4°50′ SZ, is one of the main shear zones of western Gondwana. The studied mylonites from this major shear zone, provide insights in the tectonic behavior and the geodynamical evolution of the western part of central Hoggar. These mylonites likely resulted from complex

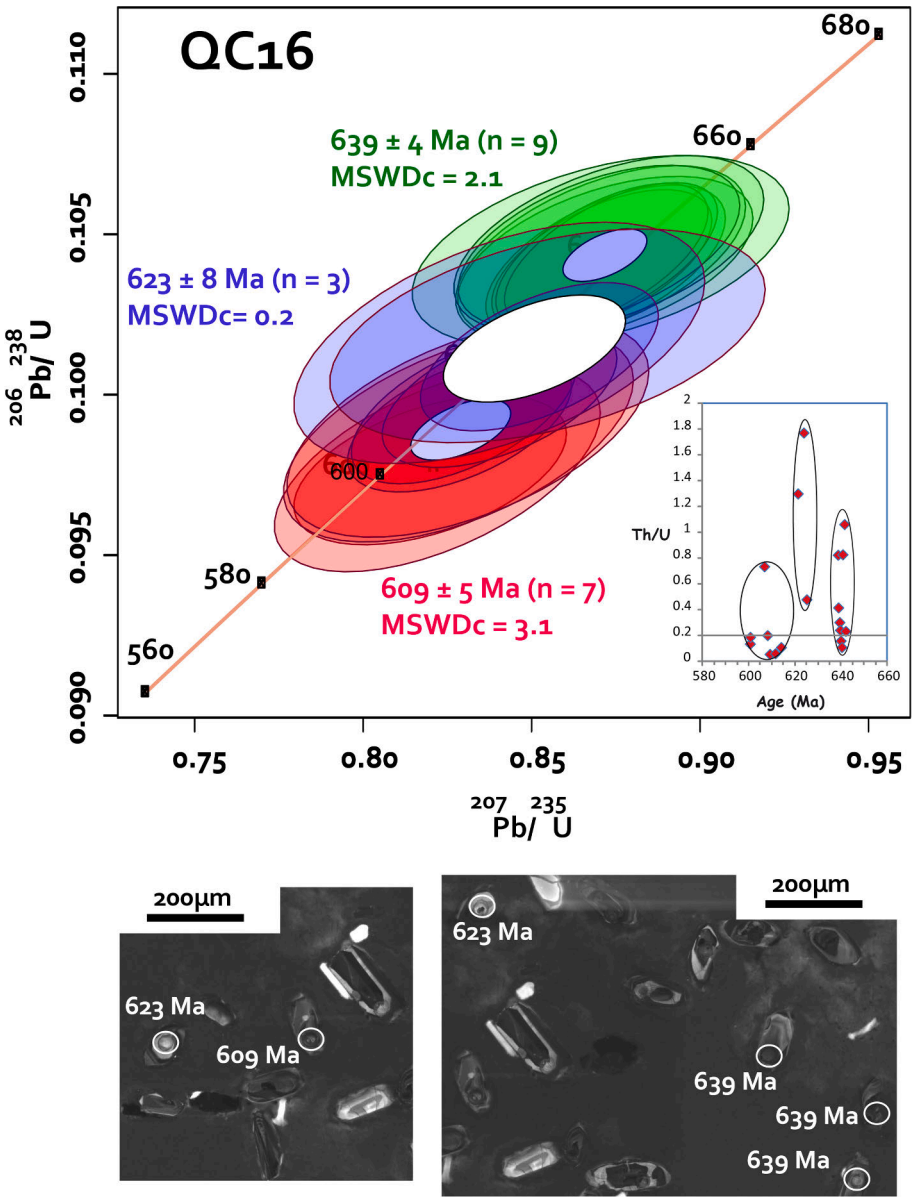

Fig. 13. U-Pb zircon concordia diagram showing the obtained ages for the QC16′ sample with some representative spotted zircon. Top: Coloured ellipses correspond to the different obtained ages of the main zircon crystals. Bottom: SEM images showing the texture of the dated zircon. The white circles indicate the spot analyses localization and the displayed ages are indicating concordia ages.

deformations of granitoids emplaced in the already active shear zone at 661 ± 2.8 Ma, 649 ± 3 Ma, and 639 ± 2 Ma. Most studied samples display plagioclase and K-feldspar crystals segregated in almost mono-mineralic layers. Minor quartz-ribbons, occasionally associated to amphibole, are usually parallel to feldspar layers but may locally crosscut the layering. In addition, quartz grains are also dispersed within feldspathic aggregates where they display an interstitial habitus and may infill fractures in feldspar. This points to a later crystallization of quartz from a fluid percolating along the already solidified feldspathic layers. Both plagioclase and K-feldspar display evidence of fluid-induced reactions: especially, plagioclase crystals are locally strongly corroded with K-feldspar crystallized in corrosion embayments and around plagioclase grains. Less frequently, K-feldspar are corroded with plagioclase infilling embayments. The feldspar layers display evidence supporting an initial dextral transcurrent solid-state deformation. Inside the ribbons, quartz grains frequently display evidence of intracrystalline deformation and an elongation oblique to the layering. This suggests moderate sinistral shearing dominantly accommodated within crystallized quartz-ribbons. Ductile deformation of the mylonites is also substantiated by the development of crystallographic fabric. Feldspars display, in most cases, a crystallographic fabric supporting dislocation creep with the activation of the [1 0 0] (0 1 0) slip system for K-feldspar and the [1 0 0] (0 0 1) slip system for plagioclase under submagmatic conditions. The quartz fabric shows a strong concentration of [0001] axis parallel to the foliation plane and orthogonal to the lineation for all the samples indicating the activation of the prismatic slip system in the < a > direction under relatively high temperature. However, stress-induced oriented crystallization may have contributed to the development of the quartz CPO since even segments of quartz ribbons cross-cutting the foliation display a similar crystallographic fabric.

In addition to emplacement ages, geochronological data have revealed two additional ages obtained from some concordant points (623 ± 8 Ma and 609 ± 4 Ma). These ages are known in the central Hoggar as a high-temperature, granulitic metamorphic event (Bertrand et al., 1986; Barbey et al., 1989; Bendaoud et al., 2008).

Altogether, these new data support a complex tectonothermal

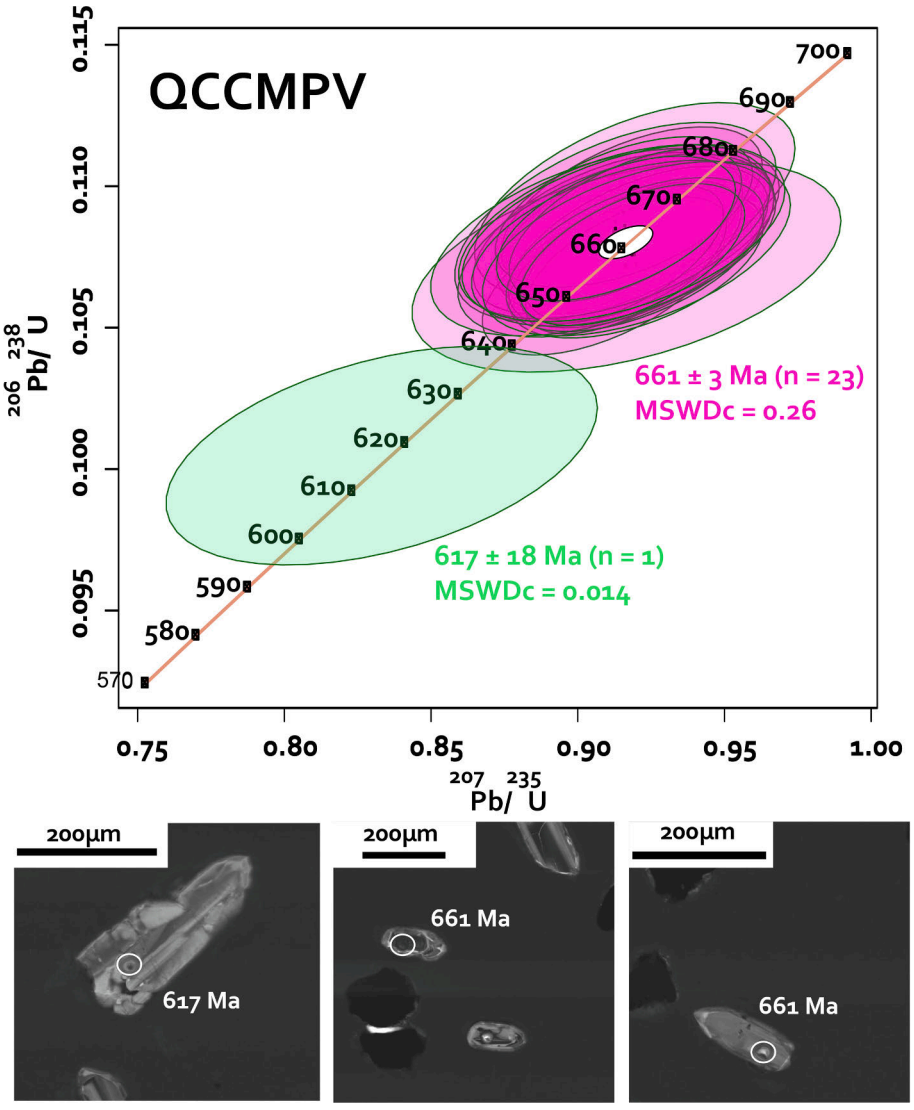

Fig. 14. U-Pb zircon concordia diagram showing the obtained ages for the QCCMPV sample with some representative spotted zircon. Top: Coloured ellipses correspond to the different obtained ages of the main zircon crystals. **Bottom:** SEM images showing the texture of the dated zircon. The white circles indicate the spot analyses localization and the displayed ages are indicating concordia ages.

evolution of the 4°50′ SZ including several successive main stages:

Granitoids resulting from partial melting of the lower crust, with or without the contribution of the uppermost mantle, were emplaced in the already active 4°50′E SZ from 661 ± 2.8 to 639 ± 2 Ma. Feldspars crystallized first and have been segregated in plagioclase and K-feldspar layers that mark the foliation. This supports that the 4°50′ SZ was active before the end of the subduction episode in western Gondwana.

These magmatic bodies underwent a solid-state ductile deformation through the activation of the Kfs [100] (010) and the plagioclase [100] (001) slip systems that triggered the dynamic recrystallization of feldspars. During this episode, it is possible that successive magma batches affected these rocks, especially if it occured during a late migmatitic episode (623 ± 4 Ma to 609 ± 2 Ma).

Still under relatively high-temperature, these mylonites locally underwent a moderate solid-state deformation through dislocation creep. This deformation, which accommodated sinistral shearing, was mainly localized in quartz ribbons in which the prismatic-<a > slip system was the dominant one.

The new structural and geochronological results obtained in this study support that the 4°50 SZ was active during subduction. This points to a model of convergence associating coeval subduction and transcurrent shearing in the intra-continental domain. Such a model is currently active in Sumatra (*e.g.,* Bellier et al., 1997) where the obliquity of the convergence is mostly accommodated by the transcurrent Great Sumatran Faults parallel to the subduction zone in which the orthogonal component of the convergence is accommodated.

CRediT authorship contribution statement

Aboubakr Deramchi: Conceptualization, Investigation, Validation, Resources, Methodology, Formal analysis, Writing – original draft, Visualization. **Alain Vauchez:** Conceptualization, Investigation, Methodology, Formal analysis, Writing – review & editing, Visualization, Supervision. **Abderrahmane Bendaoud:** Conceptualization, Investigation, Methodology, Formal analysis, Writing – review & editing, Visualization, Supervision. **Fabrício de Andrade Caxito:** Conceptualization, Investigation, Methodology, Formal analysis, Writing – review & editing, Visualization. **Zakaria Boukhalfa:** Investigation, Formal analysis, Writing – review & editing, Visualization. **Sidali Doukkari:**

Investigation, Methodology, Formal analysis, Visualization. **Saïd Maouche:** Investigation, Writing – review & editing. **Cristiano Lana:** Investigation. **Khaled Aghanbilou:** Investigation. **Abderrezak Bouzid:** Investigation, Writing – review & editing.

Declaration of Competing Interest

The authors declare that they have no known competing financial interests or personal relationships that could have appeared to influence the work reported in this paper.

Data availability

The authors do not have permission to share data.

Acknowledgment

The present-work was funded by the FP7 IRSES-MEDYNA project (*Maghreb-EU Research Staff Exchange on Geodynamics, Geohazards, and Applied Geology in northwest Africa*). This work was also elaborated under the project of "*Géodynamique Précambrienne et Phanérozoïque de la lithosphère du Hoggar à partir des données géologiques et magnétotelluriques*" which is hosted in the CRAAG Algiers research center (Centre de Recherche en Astronomie, Astrophysique et Géophysique). The geochronological analyses were funded by Instituto Serrapilheira through Project Mobile (grant Serra-1912-31510) and CNPq-Brazil through grant 408815/2021–3, both to FAC. The authors would like to thank the two reviewers Jean Paul Liégeois and Eric Ferre for their constructive reviews that enhanced the manuscript quality.

The authors would like to thank the Algerian public institutions for supporting and facilitating the development of this work (in Algiers and Tamanrasset). The authors thank the CRAAG for providing the necessary material for elaborating this work. At Geosciences Montpellier (University of Montpellier, France), we are pleased to thank Christophe Nevado and Doriane Delmas for the high quality polished thin-sections and Fabrice Barou for his support for the acquisition of EBSD measurements. We gratefully thank Andrea Tommasi, Jean-Marie Dautria, El-Hocine Fettous, Renaud Caby for the helpful discussions and suggestions, and David Mainprice for his assistance in the use of the MTex Toolbox. A special thanks to the Federal University of Ouro Preto (UFOP) for performing the geochronological analysis. The authors are grateful to Hichem Bendjelloul for his participation and help in the field.

Appendix A. Supplementary data

Supplementary data to this article can be found online at https://doi.org/10.1016/j.precamres.2023.107085.

References

Abdallah, N., Liégeois, J.P., De Waele, B., Fezaa, N., Ouabadi, A., 2007. The Temaguessine Fe-cordierite orbicular granite (Central Hoggar, Algeria): U-Pb SHRIMP age, petrology, origin and geo-dynamical consequences for the late Pan-African magmatism of the Tuareg shield. J. Afr. Earth Sc. 49, 153–178.

Acef, K., Liégeois, J.P., Ouabadi, A., Latouche, L., 2003. The Anfeg post-collisional Pan-African high-K calc-alkaline batholith (Central Hoggar, Algeria), result of the Latea microcontinent metacratonisation. J. Afr. Earth Sc. 37, 295–311.

Arab, A., Ouzegane, K., Drareni, A., Doukkari, S., Zetoutou, S., Kienast, J.R., 2014. Phase equilibria modeling of kyanite-bearing eclogitic metapelites in the NCKFMASHTO system from the Egéré terrane (Central Hoggar, South Algeria). Arab. J. Geosci. https://doi.org/10.1007/s12517-014-1413-z.

Araïbia, K., Amri, A., Amara, M., Bendaoud, A., Hamoudi, M., Pedrosa-Soares, A., De Andrade Caxito, F. Characterizing terranes and a Neoproterozoic suture zone in Central Hoggar (Tuareg Shield, Algeria) with airborne geophysics and Landsat 8 OLI data, Journal of African Earth Sciences, Volume 187, 2022, 104455, ISSN 1464-343X, https://doi.org/10.1016/j.jafrearsci.2022.104455.

Azzouni-Sekkal, A, Bonin.B, Bowden. P, Bechiri-Benmerzoug. F, Meddi. Y. 2020. Zircon U–Pb and Lu–Hf isotopic systems in ediacaran to Fortunian "Taourirt" granitic ring complexes (Silet and In Tedeini terranes, Tuareg shield, Algeria), Journal of African Earth Sciences, Elsevier, 2020, 168, pp.103865. https://DOI10.1016/j.jafrearsci.2020.103865.

Azzouni-Sekkal, A., Liégeois, J.P., Bechiri-Benmerzoug, F., Belaidi-Zinet, S., Bonin, B., 2003. The "Taourirt" magmatic province, a marker of the very end of the Pan-African orogeny in the Tuareg Shield: review of the available data and Sr-Nd isotope evidence. J. Afr. Earth Sc. 37, 331–350.

Bachmann, F., Hielscher, R., Schaeben, H., 2011. Grain detection from 2d and 3d EBSD data–specification of the MTEX algorithm. Ultramicroscopy 111 (12), 1720–1733. Bürgmann, R., Dresen, G., 2008. Rheology of the lower crust and upper mantle: evidence.

Bachmann, F., Hielscher, R., Jupp, P.E., Pantleon, W., Schaeben, S., Wegert, E., 2010. Inferential statistics of EBSD data from within individual crystalline grains. J. Appl. Cryst. 43 (2010), 1338–1355.

Barbey, P., Bertrand, J.M.L., Angoua, S., Dautel, D., 1989. Petrology and U/Pb geochronology of the Telohat migmatites, Aleksod, Central Hoggar. Algeria. Contrib. Min. 101, 207–219.

Bechiri-Benmerzoug, F., Bonin, B., Bechiri, H., Khéloui, R., Talmat-Bouzeguella, S., Bouzid, K., 2017. Hoggar geochronology: a historical review of published isotopic data. Arab. J. Geosci. 10, 351–383.

Béchiri-Benmerzoug, F., 2012. Les granitoïdes de type ttg de la région de Silet, Hoggar, Algérie: contribution à la connaissance de la structuration du bloc d'Iskel (Silet, Hoggar occidental) Algérie. Edition universitaire Européene. ISBN 13: 9783841784537.

Bellier, O., Sébrier, M., Pramumijoyo, S., Beaudouin, T., Harjono, H., Bahar, I., Forni, O., 1997. Paleoseismicity and seismic hazard along the Great Sumatran Fault (Indonesia). J. Geodyn. 24, 169–183.

Bendaoud, A., Ouzegane, K., Godard, G., Liegeois, J.P., Kienast, J.R., Bruguier, O., Drareni, A., 2008. Geochronology and meta-morphic P–T–X evolution of the Eburnean granulite-facies met-apelites of Tidjenouine (Central Hoggar, Algeria): witness of the LATEA metacratonic evolution. In: Ennih, N. and Liégeois, J.-P. (Eds) The Boundaries of the West African Craton. Geological So-ciety of London, Special Publication, 297, 111-146.

Bendaoud, A., Ouzegane, K., Kienast, J.R., 2003. Textures and phase relationships in ferrous granulites from Tidjenouine (Hoggar, Algeria): fayalite-ferrossilite-quartz secondary. J. Afr. Earth Sc. 37, 241–255.

Bendaoud, A., Derridj, A., Ouzegane, K., Kienast, J.R., 2004. Granulites of the Laouni terrane, (Tamanrasset, Tidjenouine, Tin Begane). J. Afr. Earth Sci. 39, 187–192. https://doi.org/10.1016/j.jafrearsci.2004.07.050.

Bertrand, J.-M., Michard, A., Boullier, A.-M., Dautel, D., 1986. Structure and U/Pb geochronology of Central Hoggar (Algeria): a reappraisal of its Pan-African evolution. Tectonics 5 (7), 955–972.

Bettioui, D., Liégeois, J-P., Fettous, E-H., Fezaa, N., Bruguier, O., Syn-kinematic emplacement of granitic batholith and leucogranite along the extensional detachment shear zone system of the Tin Begane area, Laouni terrane (LATEA metacraton, Central Hoggar, Algeria), Precambrian Research, Volume 368, 2022, 106484, ISSN 0301-9268, https://doi.org/10.1016/j.precamres.2021.106484.

Beuf, S., Biju-Duval, B., De Charpal, O., Rognon, P., Gariel, O., Bennacef, A., 1971. Les grès du Paléozoïque inférieur au Sahara. Publication IFP, Collection "Science et techniques du pétrole". Paris 464 pp.

Black, R., Latouche, L., Liégeois, J.P., Caby, R., Bertrand, J.M., 1994. Pan-African displaced terranes in the Tuareg shield (central Sahara). Geology 22, 641–644.

Bouchez, J.L., Delas, C., Gleizes, G., Nédélec, A., Cuney, M., 1992. Submagmatic microfractures in granites. Geology 20 (1), 35–38.

Boudjema, A., 1987. Evolution structurale du basin pétrolier "triasique'' du Sahara nord oriental (Algérie). University Paris-Sud, Thesis, p. 290.

Boukhalfa, Z., Bouzid, A., Xu, Y., Bendaoud, A., Yang, B., Hamoudi, M., Djeddi, M., 2020. Magnetotelluric investigation of the Precambrian crust and intraplate Cenozoic volcanism in the Gour Oumelalen area, Central Hoggar. South Algeria. Geophysical Journal International 223 (3), 1973–1986. https://doi.org/10.1093/gji/ggaa432.

Boullier, A.M., Bertrand, J.M., 1981. Tectonique tangentielle profonde et couloirs mylonitiques dans le Hoggar central polycyclique (Algérie). Bull. Soc. Gdol. Fr 23.

Bouzeguella-Talmat, S., 2014. Géochimie, géochronologie et contexte géodynamique des granitoïdes panafricain de l'Amsel (Hoggar. Thèse de doctorat. FSTGAT/ USTHB, Algérie, Algérie), p. 331.

Bouzid, A., Bayou, B., Liégeois, J.P., Bourouis, S., Bougchiche, S.S., Bendekken, A., Ouabadi, A., 2015. Lithospheric structure of the Atakor metacratonic volcanic swell (Hoggar, Tuareg Shield, southern Algeria): electrical constraints from magnetotelluric data. Geol. Soc. Am. Spec. Paper 514, 239–255. https://doi.org/10.1130/2015.2514(15).

Bouzid, A., Bendekken, A., Deramchi, A., Abtout, A., Akacem, N., Djeddi, M., Hamoudi, M., et al., 2019. Electrical conductivity constraints on the geometry of the Western LATEA boundary from a magnetotelluric data acquired near Tahalgha Volcanic District (Hoggar, Southern Algeria). In: Bendaoud, A. (Ed.), The Geology of the Arab World—An Overview. Springer Geology, pp. 167–196.

Bowden, P., Cottin, J.-Y., Belousova, E., Greau, W., L., Griffin, S., Y., O'reillya, A., Azzouni-Sekkal, A., Remaci-Benouda, N., and Bechiri-Benmerzoug, F., 2014. Ediacaran granites in the Tuareg shield, West Africa: alkalinity and end-Gondwanan assembly Goldschmidt2014 Abstracts.

Brahimi, S., Liégeois, J.P., Ghienne, J.F., Munshy, M., Bourmatte, A., 2018. The Tuareg shield terranes revisited and extended towards the northern Gondwana margin: Magnetic and gravimetric constraints. Earth Sci. Rev. 185, 572–599.

Bruguier, O., Caby, R., Bosch, D., Ouzegane, K., Deloule, E., Dhuime, B., Bendaoud, A., Kienast, J.R., 2020. A case study of in situ analyses (major and trace elements, U-Pb geochronology and Hf-O isotopes) of a zircon megacryst: Implication for the evolution of the Egéré terrane (Central Hoggar, Tuareg Shield, Algeria). Precambr. Res. 351, 105966 https://doi.org/10.1016/j.precamres.2020.105966.

Caby, R., Andreopoulos-Renaud, U., Gravelle, M., 1982. Cadre géologique et géochronologie U/Pb sur zircon des batholites précoces dans le segment pan-africain

du Hoggar central (Algérie). Bulletin de la Société Géologique de France 24, 677–684.
Caxito, F.D.A., Santos, L.C.M.D.L., Ganade, C.E., Bendaoud, A., Fettous, E.H., Bouyo, M. H., 2020. Toward an integrated model of geological evolution for NE Brazil-NW Africa: The Borborema Province and its connections to the Trans-Saharan (Benino-Nigerian and Tuareg shields) and Central African orogens. Brazilian J. Geol. 50 (2).
Chen, J., Zhenmin, J., Liu, W., Wang, Y., Zhang, J. Rheology of dry K-feldspar aggregates at high temperature and high pressure: An experimental study, Tectonophysics, Volume 817, 2021, 229072, ISSN 0040-1951, https://doi.org/10.1016/j.tecto.2021.229072.
Cordani, U.G., Pimentel, M.M., Ganade de Araújo, C.E., Fuck, R.A., 2013. The significance of the Transbrasiliano-Kandi tectonic corridor for the amalgamation of Western Gondwana: Brazilian. J. Geol. 43 (3), 583–597. https://doi.org/10.5327/Z2317-48892013000300012.
da Silva Amaral, W., dos Santos, F.H., Braga, L.R.C., Pitombeira, J.P.A., de Sousa, D.F.M., Fuck, R.A., da Costa, F.G., 2023. Paleoproterozoic crustal evolution of the northern Borborema Province, NE Brazil: Insights from high-grade metamorphic rocks of the Canindé do Ceará Complex. Precambr. Res. 384, 106941 https://doi.org/10.1016/j.precamres.2022.106941.
Deramchi, A., Bouzid, A., Bendaoud, A., Ritter, O., Hamoudi, M., Cruces-Zabala, J., Meqbel, N., Boukhalfa, Z., Boughchiche, S.S., Abtout, A., Boukhlouf, W., Bendekken, A., 2020. Neoproterozoic amalgamation and Phanerozoic reactivation of Central/Western Hoggar (Southern Algeria, Tuareg Shield) lithosphere imaging using Magnetotelluric data. J. Geodyn. https://doi.org/10.1016/j.jog.2020.101764.
Djouadi, M.T., Gleizes, G., Ferré, E., Bouchez, J.L., Caby, R., Lesquer, A., 1997. Oblique magmatic structures of two epizonal granite plutons, Hoggar, Algeria: late-orogenic emplacement in a transcurrent orogen. Tectonophysics 279 (1–4), 351–374.
Doukkari, S.A., Ouzegane, K., Godard, G., Diener, J.F.A., Kienast, J.-R., Liégeois, J.-P., Arab, A., Drareni, A., 2015. Prograde and retrograde evolution of eclogite from Adrar Izzilatène (Egéré-Aleksod terrane, Hoggar, Algeria) determined from chemical zoning and pseudosections, with geodynamic implications. Lithos 226, 217–232. Ferreira, V.P., Sial, A.N., Pimentel, M.M., Moura, C.A.V., 2004.
Doukkari, S.A., Ouzegane, K., Arab, A., Kienast, J.R., Godard, G., Drareni, A., Zetoutou, S., Liégeois, J.P., 2014. Phase relationships and P-T path in NCFMASHTO system of the eclogite from the Tighsi area (Egéré terrane, Central Hoggar, Algeria). J. Afr. Earth Sc. 99, 276–286.
Ferré, E., Déléris, J., Bouchez, J.L., Lar, A.U., Peucat, J.J., 1996. The Pan-African reactivation of Eburnean and Archaean provinces in Nigeria: structural and isotopic data. J. Geol. Soc. London 153 (5), 719–728.
Ferré, E., Gleizes, G., Caby, R., 2002. Obliquely convergent tectonics and granite emplacement in the Trans-Saharan belt of Eastern Nigeria: a synthesis. Precambr. Res. 114 (3–4), 199–219.
Fettous, E.H., 2016. Le Paléoprotérozoïque dans le Hoggar occidental et central et son évolution post-éburnéenne. Unpublished Thesis. FSTGAT/USTHB. Algérie, 500 p.
Ganade de Araujo, C.E., Rubatto, D., Hermann, J., Cordani, U.G., Caby, R., Basei, M.A., 2014. Ediacaran 2,500-km-long synchronous deep continental subduction in the West Gondwana Orogen. Nature https://doi.org/10.83/ncomms6198.
Gerdes, A., Zeh, A., 2006. Combined U-Pb and Hf isotope LA-(MC-) ICP-MS analyses of detrital zircon: comparison with SHRIMP and new constraints for the provenance and age of an Armorican metasediment in Central Germany. Earth Planet. Sci. Lett. 249, 47–62.
Gerdes, A., Zeh, A., 2009. Zircon formation versus zircon alteration—new insights from combined U-Pb and Lu–Hf in-situ LA-ICP-MS analyses, and consequences for the interpretation of Archean zircon from the Central Zone of the Limpopo Belt. Chem. Geol. 261 (3–4), 230–243. https://doi.org/10.1016/j.chemgeo.2008.03.005.
Good, N., De Wit, M.J., 1997. The Thabazimbi-Murchison lineament of the Kaapvaal craton, South Africa: 2700 Ma of episodic deformation. J. Geol. Soc. London 154 (1), 93–97. https://doi.org/10.1144/gsjgs.154.1.0093.
Guiraud, R., Bosworth, W., Thierry, J., Delplanque, A., 2005. Phanerozoic geological evolution of Northern and Central Africa: An overview. J. Afr. Earth Sci. 43, 83–143.
Hasalová, P., Janousek, ˇ V., Schulmann, K., Stípská, ˇ P., Erban, V., 2008. From orthogneiss to migmatite: geochemical assessment of the melt infiltration model in the Gföhl Unit (Moldanubian Zone, Bohemian Massif). Lithos 102, 508–537.
Henry, B., Derder, M.E.M., Bayou, B., Guemache, M.A., Nouar, O., Ouabadi, A., Djellit, H., Amenna, M., Hemmi, A., 2008. Inhomogeneous shearing related with rocks composition: evidence from a major late-Pan-African shear zone in the Tuareg shield (Algeria). Swiss J Geosci 101, 453–464. https://doi.org/10.1007/s00015-008-1262-4.
Henry, B., Derder, M.E., Maouche, S., Nouar, O., Amenna, M., Bayou, B., & Ouabadi, A. (2018). An Overview of the Plutons Magnetic Fabric Studies in the Hoggar Shield: Evolution of the Major Shear Zones during the Pan-African. The Geology of the Arab World—An Overview.
Hielscher, R., Schaeben, H., 2008. a novel pole figure inversion method: Specification of the MTEX algorithm. J. Appl. Crystallogr. 41, 1024–1037.
Jackson, S.E., Pearson, N.J., Griffin, W.L., Belousova, E.A., 2004. The application of laser ablation-inductively coupled plasma-mass spectrometry to in situ U-Pb zircon geochronology. Chem. Geol. 211 (1–2), 47–69. https://doi.org/10.1016/j.chemgeo.2004.06.017.
Fettous et al., 2018. L'exhumation tardi-orogénique du terrane de Laouni, Latea, Bouclier Touareg, Algérie. 27th Colloquium of African Geology /17th Conference of the Geological Society of Africa (CAG27), July 21 – 28, Aveiro, Portugal.
Le Pichon, X., 1968. Sea-floor spreading and continental drift. J. Geophys. Res. 73 (12), 3661–3697.
Liégeois, J.P., Benhallou, A., Azzouni-Sekkal, A., Yahiaoui, R., Bonin, B., 2005. The Hoggar swell and volcanism: reactivation of the Precambrian Tuareg shield during Alpine convergence and West African Cenozoic volcanism. In: In: Foulger, G.R., Natland, J.H., Presnall, D.C., Anderson, D.L. (Eds.), Plates, Plumes and Paradigms, Geological Society of America Special Paper Vol. 388. pp. 379–400.
Liégeois, J.P., Latouche, L., Boughrara, M., Navez, J., Guiraud, M., 2003. The LATEA metacraton (Central Hoggar, Tuareg shield, Algeria): behavior of an old passive margin during the Pan-African orogeny. J. Afr. Earth Sc. 37, 161–190.
Liégeois, J.-P 2019. A New Synthetic Geological Map of the Tuareg Shield: An Overview of Its Global Structure and Geological Evolution. In, A. Bendaoud et al. (eds.), The Geology of the Arab World—An Overview, Springer Geology, https://doi.org/10.1007/978-3-319-96794-3_2, 83-107.
Mainprice, D., Bachmann, F., Hielscher, R., Schaeben, H., 2014. Calculating anisotropic piezoelectric properties from texture data using the MTEX open source package. Geol. Soc. London, Spec. Publ. 409 https://doi.org/10.1144/SP409.2.
Montardi, Y., Mainprice, D., 1987. A TEM study of the natural plastic deformation of calcic plagioclase (A 68–70). Bull. Mineral. 110, 1–14.
Nouar, O., B. Henry, J.P. Liégeois, M. Amenna, N. Abdallah, M.E.M. Derder, M. Ayache, Late Pan-African Murzuq event in the Central Hoggar: Sinistral displacement along the Ounane major shear zone (Gour Oumelalen, Algeria) shown by the magnetic fabric of the Tissellíline pluton, Journal of African Earth Sciences, Volume 184, 2021, 104333, ISSN 1464-343X, https://doi.org/10.1016/j.jafrearsci.2021.104333.
Ouadahi, S., Bendaoud, A., Bodinier, J.L., Dautria, J.M., Vauchez, A., Fettous, E.H., Alard, O., 2022. A suture related accretionary wedge in the Gondwana assembly: Insights from serpentinites in the Hoggar shield. Algeria. *Precambrian Research* 369, 106505. https://doi.org/10.1016/j.precamres.2021.106505.
Rougier, S., Missenard, Y., Gautheron, C., Barbarand, J., Zeyen, H., Pinna, R., Liégeois, J. P., Bonin, B., Ouabadi, A., Derder, M.E.M., Frizon de Lamotte, D., 2013. Eocene exhumation of the Tuareg Shield (Sahara, Africa). Geology 41, 615–618. https://doi.org/10.1130/G33731.1.
Santos, F.H., Amaral, W.S., Uchôa, F.E., Martins, D.T., 2017. Detrital zircon U-Pb ages and whole-rock geochemistry of the Neoproterozoic Paulistana and Santa Filomena complexes, Borborema Province, northeastern Brazil: implications for source area composition, provenance, and tectonic setting. Int. Geol. Rev. 59 (15), 1861–1884. https://doi.org/10.1080/00206814.2017.1300074.
Santos, L.C.M.L., Dantas, E.L., Santos, E.J., Santos, R.V., Lima, H.M., 2015. Early to late Paleoproterozoic magmatism in NE Brazil: The Alto Moxotó Terrane and its tectonic implications for the pre-West Gondwana assembly. J. South Amer. Earth Sci. 58, 188–209. https://doi.org/10.1016/j.jsames.2014.07.006.
Sautter, V., 1986. Les éclogites de 1'Aleksod (sud algérien): des témoins in situ d'une collision intracontinentale. J. Afr. Earth Sci. 5, 345–357.
Sláma, J., Košler, J., Condon, D.J., Crowley, J.L., Gerdes, A., Hanchar, J.M., Whitehouse, M.J., 2008. Plešovice zircon—a new natural reference material for U-Pb and Hf isotopic microanalysis. Chem. Geol. 249 (1–2), 1–35. https://doi.org/10.1016/j.chemgeo.2007.11.005.
Stacey, J.S., Kramers, J.D., 1975. Approximation of terrestrial lead. Isotope evolution by a two-stage model. Earth Planet. Sci. Lett. 26 (2), 207–221. https://doi.org/10.1016/0012-821X(75)90088-6.
Stipp, M., Stünitz, H., Heilbronner, R., Schmid, S.M., 2002. The eastern Tonale fault zone: A "natural laboratory" for crystal plastic deformation of quartz over a temperature range from 250 to 700 C. J. Struct. Geol. 24, 1861–1884.
Stünitz, H., Fitz Gerald, J.D., Tullis, J., 2003. Dislocation generation, slip systems, and dynamic recrystallization in experimentally deformed plagioclase single crystals. Tectonophysics 372, 215–233. https://doi.org/10.1016/S0040-1951(03)00241-5.
Tommasi, A., Vauchez, A., Fernandes, L.A.D., Porcher, C.C., 1994. Magma-assisted strain localization in an orogen-parallel transcurrent shear zone of southern Brazil. Tectonics 13, 421–437.
Van Achterbergh, E., Griffin, W.L., Stiefenhofer, J., 2001. Metasomatism in mantle xenoliths from the Letlhakane kimberlites: estimation of element fluxes. Contrib. Miner. Petrol. 141 (4), 397–414. https://doi.org/10.1007/s004100000236.
Vauchez, A., Tommasi, A., 2003. Wrench faults down to the asthenosphere: geological and geophysical evidence and thermo-mechanical effects. In: Storti, F., Holdsworth, R.E., Salvini, F. (Eds.), Intraplate strike-slip deformation belts. Special Publication, 210. Geological Society of London, pp. 15–34. https://doi.org/10.1144/GSL.SP.2003.210.01.02.
Vauchez, A., Pacheco-Neves, S., Caby, R., Corsini, M., Egydio-Silva, M., Arthaud, M., Amaro, V., 1995. The Borborema shear zone system. J. S. Am. Earth Sci. 8, 247–266. https://doi.org/10.1016/0895-9811(95)00012-5.
Vauchez, A., Tommasi, A., Mainprice, D., 2012. Faults (shear zones) in the Earth's mantle. Tectonophysics 558–559, 1–27. https://doi.org/10.1016/j.tecto.2012.06.006.